Topics in Millimeter-Wave Imaging Arrays

Thesis by

Dayalan P. Kasilingam

In Partial Fulfillment of the Requirements

for the Degree of

Doctor of Philosophy

California Institute of Technology,

Pasadena, California

1987

(Submitted December 29, 1986.)

TO MY PARENTS

தொட்டனைத் தூறும் மணற்கேணி மாந்தற்குக்
கற்றனைத் தூறும் அறிவு.

Acknowledgements

There are several people I would like to thank for making this thesis possible. I would like to start by thanking my advisor Dr. David Rutledge for his guidance and support throughout my stay at Caltech. His motivation has been a great inspiration to me both professionally and personally. I would like to thank Professors William Bridges, Charles Papas, Demetri Psaltis and Yaser Abu-Mostafa for taking the time to be on by dissertation committee. I would also like to thank all the members (past and present) of the millimeter-wave integrated-circuits group for their constant support which made my work at Caltech that much more interesting.

I am also grateful to the members of the masters class of 1982 for the help and encouragement I received during my masters degree and the period after. I am also indebted to Ms. Joyce Liddell and Ms. Linda Dozsa for keeping things moving in Steele. The constant support of my friends made the difficult periods at Caltech more bearable. Therefore I would like to say a big thank you to all my friends, too numerous to mention by name. I would also like to say a very special thank you to my brother Arjuna, who brought a piece of home to my stay in the United States.

Last but not least I would like to thank Caltech for supporting me financially during my stay here.

Topics in Millimeter-Wave Imaging Arrays

Abstract

In this thesis two different types of antenna arrays are investigated as possible configurations for *two-dimensional* diffraction limited imaging arrays. The first configuration is the "fly's-eye" array of microlenses. It is shown that this configuration may be utilized to achieve diffraction limited imaging with theoretical coupling efficiencies of around 50%. The other configuration is the two-dimensional horn array. It is shown that in this configuration, wide-angled horns etched into silicon achieve theoretical coupling efficiencies of 60%. A design for a *two-dimensional* imaging array, using horn elements of aperture size $1.5\lambda_0$ was suggested. Also covered in this thesis are the radiation losses and the substrate-mode losses of coplanar transmission lines. It is shown that at millimeter-wave frequencies these losses are prohibitively high. Finally in the appendix a simulation of Schottky diode mixers is described as a possible design tool for analyzing millimeter-wave detector circuits.

TABLE OF CONTENTS.

CHAPTER 1

Introduction

1.1 Millimeter-Waves

The millimeter-wave region is generally defined as the frequency region from 30 to 300 GHz. Millimeter-wave characteristics differ from those of microwave and infrared, and these differences make millimeter-wave systems more suitable for certain applications. In recent years the millimeter-wave region has seen significant advances in the development of transmitters, receivers [1–2], sources [3–4], devices [5–8] and components [9–10]. The current resurgence of interest arises from the limitations of infrared and optical systems and the overcrowding of the microwave spectrum. However, performance, reliability and cost have impeded the widespread use of these wavelengths. Therefore considerable research is required to make millimeter-wave systems competitive with infrared and microwave systems which are based on relatively mature technology.

Short wavelength, large bandwidth and atmospheric propagation effects determine the application of millimeter-wave systems. The short wavelength allows the use of components with considerably reduced size. The advent of integrated-circuit technology has not only enabled the fabrication of smaller components, it has also introduced the concept of monolithic circuits to millimeter-wave systems. This is highly desirable for missiles, satellites and aircraft. The short wavelength also results in narrower antenna beamwidth. It provides greater resolution and precision in tracking and discrimination. The narrow beamwidth also gives higher gain and greater immunity to jamming.

The large bandwidth provides higher information rate capability, wide-band spread spectrum capability and large Doppler shifts. In radar applications these

characteristics result in high immunity to jamming and interference and greater sensitivity in areas such as range resolution, detection and target signature. The atmospheric attenuation and losses are relatively low in the transmission windows compared to infrared and optical frequencies. Lower attenuation in aerosols, dust and smoke make millimeter-wave radars and radiometers much more effective than their optical and infrared competitors. The principal application of millimeter-wave technology has been in communications [11], radar [12], radiometry [13], remote sensing [14], missile guidance [15] and radio astronomy [16]. Millimeter-waves have also been used in spectroscopy and biological applications.

1.2 Millimeter-Wave Imaging Arrays

Scanned millimeter-wave imaging systems have been made with antenna arrays. Hollinger *et al.* [17], Hodges *et al.* [18], Waldman *et al.* [19] have designed and implemented such systems. Scanning systems, whether they are electronic or mechanical, cannot image rapidly moving objects or changing scenes. This is because the system sees only one pixel at a time. As the total time taken is the product of the number of pixels and the integration time, this forces one to use short integration times. Short integration times result in poor noise performance. The way to circumvent this limitation is to image all points simultaneously onto multiple sensors. An array of detectors with associated antennas is a possible configuration.

Evaporography and pyroelectric vidicons have been used as image plane devices [20]. But like all large area thermal detectors, they suffer from low speed and significant crosstalk. The need for sensitive and fast detection has required the development of antenna arrays. High-speed detectors such as SIS junction detectors [21], Schottky diodes [22], and microbolometers [23] have been developed in recent years. These developments coupled with integrated-circuit technology

should facilitate the fabrication of *two-dimensional* focal plane imaging arrays.

Several focal plane imaging systems based on single-mode antenna arrays and multi-mode antenna arrays have been built. Fig. 1.1 shows multi-mode imaging and single-mode imaging. In single-mode arrays each point on the target is imaged onto a separate element of the array. Properly designed single-mode systems may achieve diffraction limited imaging. Diffraction limited imaging is the term used to refer to an imaging system whose resolution is limited by the resolution of the optical system. It can been shown that diffraction limited resolution may be achieved only if the antenna array is able to spatially sample the image above a minimum rate defined by the optical system. In multi-mode arrays the antenna array acts as a single receptor. Therefore these systems are suitable only for objects that require low spatial resolution. Rutledge and Schwarz [24] built a high detectivity multi-mode antenna array at 215 GHz.

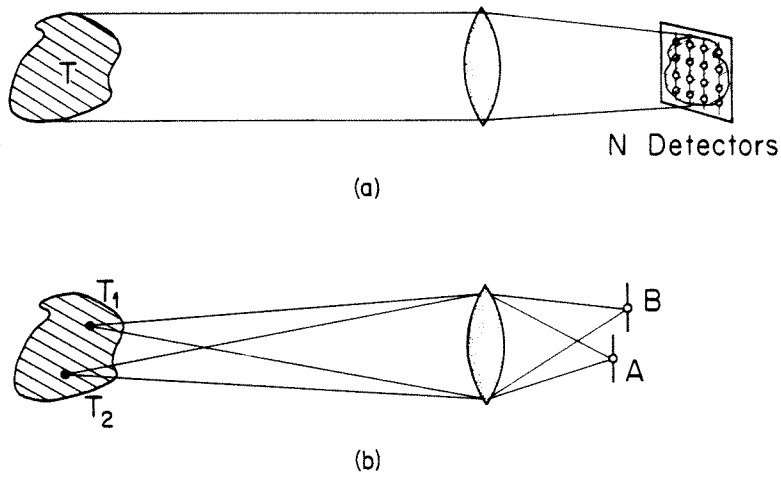

Figure 1.1 (a) Multi-mode antenna array (b) Single-mode antennas for high resolution imaging.

Several *one-dimensional* imaging arrays have been built [25-26] to do diffraction limited and close to diffraction limited imaging. Quasi-optical systems [27]

with lens-coupled antennas are used in many of these systems. Fig. 1.2 shows a quasi-optical system with a lens-coupled antenna array. Microstrip antennas [28], V antennas [29], slots, dipoles and bowties [30] are some of the many planar antennas that have been used in these arrays. Several different types of transmission lines and waveguides [31] have also been used in substrate and lens-coupled circuits. Their performance strongly influences the overall performance of the system. Schottky diodes, SIS junctions and microbolometers have been used as detectors for different applications. The SIS junctions has the highest sensitivity but it requires cryogenic operation. They are best suited for millimeter and submillimeter radio astronomy [32] where high sensitivity is a must. The microbolometers are easy to fabricate but their response time is limited to microseconds. They have been used successfully in submillimeter-wave imaging arrays [25]. The Schottky diode is difficult to fabricate. But they have excellent high frequency performance and are ideal for room temperature millimeter-wave work.

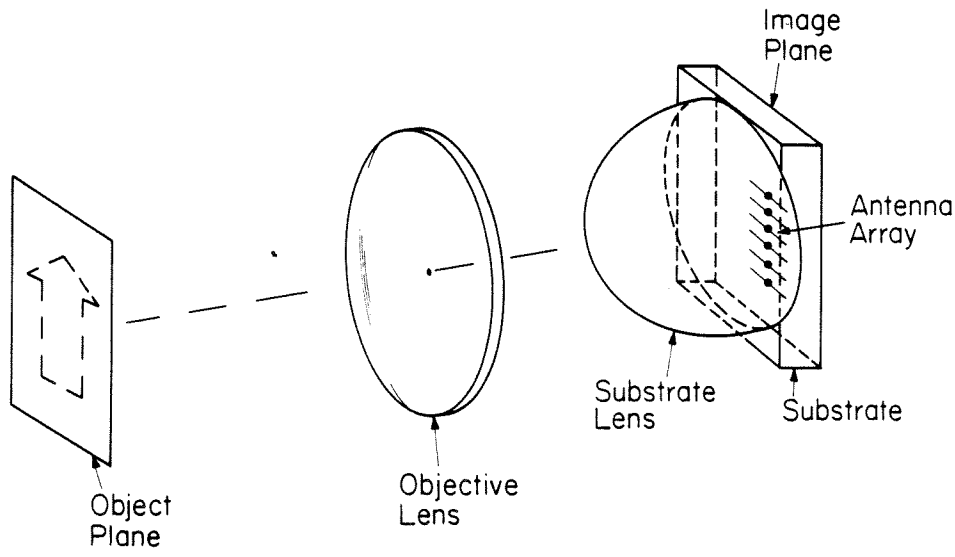

Figure 1.2 Quasi-optical imaging system with substrate lens-coupled antenna array.

1.3 Prospects for Two-Dimensional Imaging Arrays

In implementing *one-dimensional* imaging arrays the low-frequency leads did not cause a problem. But in *two-dimensional* arrays they are much harder to fabricate because of the shortage of space [33]. In a nutshell the problem is how does one build a *two-dimensional* imaging array so that the antennas are close enough to achieve diffraction limited imaging and at the same time run low-frequency connections to each antenna. In the *two-dimensional* tracking array built by Tong *et al.* [34], the array is partially multi-mode and therefore does not require low-frequency leads for each antenna. The solution is to make smaller antennas. But smaller antennas have smaller effective areas and therefore do not couple power efficiently. In this work, I discuss two possible ways of increasing the effective area of the receiving antennas while maintaining diffraction limited imaging.

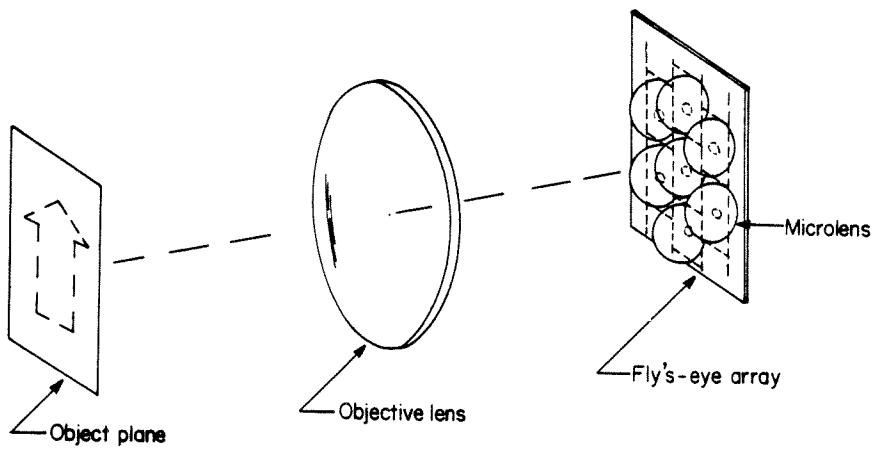

Figure 1.3 Fly's eye array of microlenses for diffraction limited imaging.

The first method is to build an array of microlenses in a "fly's eye" configuration as shown in Fig. 1.3. The lenses will be small enough to achieve diffraction limited imaging. Each lens will have its associated antenna which will be physically a lot smaller than the lens itself. The hope is that the microlens will increase

the effective area of the antenna to the size of the lens. The absorption losses due to the lens material may also be reduced considerably.

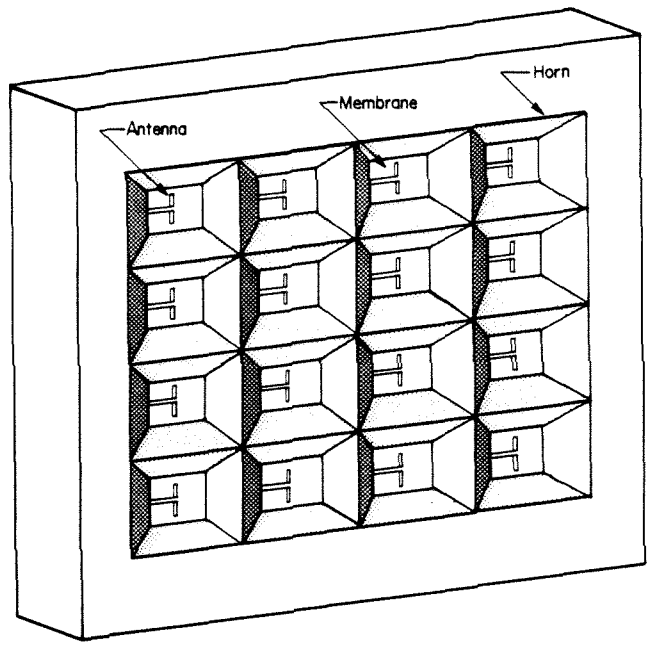

Figure 1.4 *Two-dimensional* imaging horn array for diffraction limited imaging.

The next configuration is the *two-dimensional* array of horns. Fig. 1.4 shows such an array. The advent of integrated-circuit technology has made this possible. The idea is to etch crystalline silicon along its $\langle 111 \rangle$ plane so as to produce a pyramidal horn like structure. The silicon will be highly doped to make the walls look 'metallic'. The receiving antenna will be built on a thin silicon nitride membrane inside the horn. Again due to the focusing effect of the horn the antenna itself does not have to be large. The extra space on the membrane surface may be utilized for running low-frequency lines. This system does not use a lens and may also be used at far-infrared frequencies where the dielectric absorption is prohibitively high.

1.4 Overview of the Thesis

The major goal is to investigate suitable configurations for *two-dimensional* imaging arrays. The above mentioned configurations are treated in Chapters 4 and 5. Chapters 2 and 3 deal with the losses of microstrip lines and coplanar transmission lines. In Chapter 2 substrate-mode losses of transmission lines on thin substrates is studied. These losses are due to power from the transmission lines coupling into extraneous substrate-modes within the dielectric. The dispersion properties of these lines are also investigated. It is important to know when the substrate-modes turn on because the substrate-mode losses are prohibitively large at millimeter-wave frequencies. In Chapter 3 the radiation loss of transmission lines on thick substrates is studied. The performance of antennas on thick substrates is also reviewed in this chapter. It is useful to know the performance of antennas and transmission lines on thick substrates because many imaging systems utilize lens-coupled systems. Parts of this work were published as a chapter in *Infrared and Millimeter Waves* [10].

In Chapter 4, the focusing properties of microlenses are investigated. As mentioned before, to achieve diffraction limited imaging it is important that the lenses be placed at close proximity to each other. This would require that the lens radius be of the order of a free space wavelength. Lenses as small as these may not necessarily focus the incident radiation. In this chapter the focusing properties of spherical lenses are analyzed rigorously so as to determine the minimum radii of lenses of different dielectric materials. The losses of these lenses are also studied to predict the improvement in absorption losses due to the reduction in size. This work was published in the *International Journal of Infrared and Millimeter Waves* [35].

In Chapter 5 the imaging properties of horn arrays are studied. As in the

case of the small lenses a rigorous solution is required because standard solutions based on diffraction theory do not apply for arrays of small horns. The chapter begins with an analysis of *one-dimensional* groove type arrays. The section on one-dimensional grooves is included to test the validity of the stepped waveguide method which is used later to analyze pyramidal horns. The comparison of this method with the cylindrical wave function method gives one insight into the accuracy of the stepped waveguide method. In the next section arrays of pyramidal horns are analyzed. The primary objective of this chapter is to design a *two-dimensional* horn array. The elemental gain and radiation pattern of these arrays are given along with the antenna coupling efficiency. The chapter ends with a possible design of a *two-dimensional* imaging horn array.

The appendix describes the program that simulates Schottky diode mixer circuits and predicts the conversion loss and noise temperature of the mixer. This analysis was conducted because of a necessity for theoretical predictions for the performance of planar Schottky diode imaging arrays built by my colleague Chung-en Zah [36]. This program is based on Held and Kerr's excellent paper [37] on the analysis of Schottky diode mixer circuits and its implementation by Siegel [38]. This appendix gives a summary of the performance of different Schottky diode mixer circuits and concludes with a comparison with experimental results obtained by Zah.

References

[1] D. P. Woody, R. E. Miller, M. J. Wengler, "85-115 GHz Receivers for Radio Astronomy," *IEEE Trans. Microwave Theory Tech.*, **MTT-33**, pp. 90–95, 1985.

[2] N. R. Erickson, "A 200-300 GHz Heterodyne Receiver," *IEEE Trans. Microwave Theory Tech.*, **MTT-29**, pp. 557–561, 1981.

[3] R. W. Mcmillan, "Near-Millimeter-Wave Sources of Radiation," *Proc. IEEE*, **73**, pp. 86–108, 1985.

[4] N. B. Kramer, "Sources of Millimeter-Wave Radiation: Traveling-Wave Tube and Solid State Sources," *Infrared and Millimeter Waves*, **4**, pp. 151–198, K. J. Button, ed., Academic Press Inc., New York, 1981.

[5] J. W. Archer, "Millimeter Wavelength Frequency Multipliers," *IEEE Trans. Microwave Theory Tech.*, **MTT-29**, pp. 552–557, 1981.

[6] N. B. Kramer, "Millimeter-Wave Semiconductor Devices," *IEEE Trans. Microwave Theory Tech.*, **MTT-24**, pp. 685–691, 1976.

[7] P. Bhartia, I. J. Bahl, *Millimeter Wave Engineering and Applications*, John Wiley and Sons, New York, 1984.

[8] J. V. DiLorenzo, D. D. Khandelwal, *GaAs FET Principles and Technology*, Artech House, Dedham MA., 1982.

[9] T. Itoh, J. Rivera, "A Comparative Study of Millimeter Wave Transmission Lines," *Infrared and Millimeter Waves*, **9**, pp. 95–132, K. J. Button, ed., Academic Press Inc., New York, 1983.

[10] D. B. Rutledge, D. P. Neikirk, D. P. Kasilingam, "Integrated Circuit Antennas," *Infrared and Millimeter Waves*, **10**, pp. 1–90, K. J. Button, ed., Academic Press Inc., New York, 1983.

[11] K. Miyauchi, "Millimeter-Wave Communications," *Infrared and Millimeter*

Waves, **9**, pp. 1–94, K. J. Button, ed., Academic Press Inc., New York, 1983.

[12] E. K. Reedy, G. W. Ewell, "Millimeter Radar," *Infrared and Millimeter Waves*, **4**, pp. 23–94, K. J. Button, ed., Academic Press Inc., New York, 1981.

[13] W. J. Wilson *et al.*, "Millimeter-Wave Imaging Sensor," *IEEE Trans. Microwave Theory Tech.*, **MTT-34**, pp. 1026–1035, 1986.

[14] E. E. Altshuler, "Millimeter-Wave Propagation and Remote Sensing of the Atmosphere," *Infrared and Millimeter Waves*, **9**, pp. 177–240, K. J. Button, ed., Academic Press Inc., New York, 1983.

[15] C. R. Seashore, "Missile Guidance," *Infrared and Millimeter Waves*, **4**, pp. 95–150, K. J. Button, ed., Academic Press Inc., New York, 1981.

[16] T. G. Phillips, K. B. Jefferts, "Millimeter-Wave Receivers and Their Applications in Radio Astronomy," *IEEE Trans. Microwave Theory Tech.*, **MTT-22**, pp. 1290–1292, 1974.

[17] J. P. Hollinger *et al.*, "A Versatile Millimeter-Wave Imaging System," *IEEE Trans. Microwave Theory Tech.*, **MTT-24**, pp. 786–793, 1976.

[18] D. T. Hodges *et al.*, "Near-Millimeter Wave Radiometric Imaging," 4th Int. Conf. on Infrared and Millimeter Waves and Their Appl., pp. 51, 1979.

[19] J. Waldman *et al.*, "Submillimeter Model Measurements and Their Applications to Millimeter Radar Systems," 4th Int. Conf. on Infrared and Millimeter Waves and Their Appl., pp. 49–50, 1979.

[20] G. Dodel, W. Kunz, "Evaporagraphic and Pyroelectric Image Recording for Two-Dimensional Plasma Interferometry in the Far-Infrared," *J. Opt. Soc. Am.*, **67**, pp. 975–978, 1977.

[21] P. L. Richards *et al.*, "Quasi Particle Heterodyne Mixing in SIS Tunnel Junctions," *Appl. Phys. Lett.*, **34**, pp. 345–347, 1979.

[22] M. V. Schneider, "Metal-Semiconductor Junctions as Frequency Converters," *Infrared and Millimeter Waves*, **6**, pp. 209–276, K. J. Button, ed., Academic Press Inc., 1982.

[23] D. P. Neikirk, " Integrated Detector Arrays for High Resolution Far-Infrared Imaging," *PhD. Thesis Dissertation*, California Institute of Technology, Pasadena, 1983.

[24] D. B. Rutledge, S. E. Schwarz, "Planar Multimode Detector Arrays for Infrared and Millimeter-Wave Applications," *IEEE J. Quantum Electron.*, **QE-17**, pp. 407–414, 1981.

[25] D. P. Neikirk *et al.*, "Far-Infrared Imaging Antenna Arrays," *Appl. Phys. Lett.*, **40**, pp. 203–205, 1982.

[26] D. P. Rutledge, M. S. Muha, "Imaging Antenna Arrays," *IEEE Trans. Antennas Propagat.*, **AP-30**, pp. 535–540, 1982.

[27] P. F. Goldsmith, "Quasi-Optical Techniques at Millimeter and Submillimeter Wavelengths," *Infrared and Millimeter Waves*, **6**, pp. 277–343, K. J. Button ed., Academic Press Inc., 1982.

[28] I. J. Bahl, P. Bhartia, *Microstrip Antennas*, Artech House, Dedham MA., 1982.

[29] D. B. Rutledge *et al.*, "Antennas and Waveguides for Far-Infrared Integrated Circuits," *IEEE J. Quantum Electron.*, **QE-16**, pp. 508–515, 1980.

[30] R. C. Compton *et al.*, "Bow-Tie Antennas on a Dielectric Half-Space: Theory and Experiment," submitted for publication *IEEE Antennas Propagat.*

[31] T. Itoh, "Dielectric Waveguide-Type Millimeter-Wave Integrated Circuits," *Infrared and Millimeter Waves*, **4**, pp. 199–274, K. J. Button, ed., Academic Press Inc., New York, 1981.

[32] M. J. Wengler *et al.*, "A Low Noise Receiver for Millimeter and Submillimeter

Wavelengths," *Intl. J. of Infrared and Millimeter Waves*, **6**, pp. 689–696, 1985.

[33] R. C. Compton, G. M. Rebeiz, D. B. Rutledge, "Developments in Two-Dimensional Arrays," *10th Intl. Conf. on Infrared and Millimeter Waves*, pp. 277–278, 1985.

[34] P. P. Tong *et al.*, "Tracking Antenna Array for Near-Millimeter-Waves," *IEEE Trans. Antennas Propagat.*, **AP-31**, pp. 512–515, 1983.

[35] D. P. Kasilingam, D. B. Rutledge, "Focusing Properties of Small Lenses," *Intl. J. of Infrared and Millimeter Waves*, **7**, pp. 1631–1648, 1986.

[36] C. E. Zah, "Millimeter-Wave Monolithic Schottky Diode Imaging Arrays," *PhD Thesis Dissertation*, California Institute of Technology, Pasadena, 1986.

[37] D. N. Held, A. R. Kerr, "Conversion Loss and Noise of Microwave and Millimeter-Wave Mixers: Part 1 – Theory," *IEEE Trans. Microwave Theory Tech.*, **MTT-26**, pp. 49–61, 1978.

[38] P. H. Siegel, "Topics in the Optimization of Millimeter-Wave Mixers," *PhD Thesis Dissertation*, Columbia University, New York, 1984.

CHAPTER 2

Substrate-Mode Losses in Coplanar Transmission Lines

Coplanar transmission lines, along with microstrip lines, are used in microwave and millimeter-wave integrated circuits as matching elements [1–3], filters [4], couplers, and as interconnections. For instance, in a millimeter-wave imaging array, coplanar waveguides may be used to match the IF signal to the output port or to an intermediary IF amplifier. Therefore, it is imperative that these lines be of low loss and exhibit good dispersion characteristics. The latter has been covered extensively in previous work [5–12]. Losses due to lossy dielectrics and imperfect conductors have also been documented [13–17].

Substrate-mode losses are usually very small at microwave frequencies because the substrate is very thin compared to a wavelength. But at millimeter-wave frequencies the substrate thickness can be comparable to the wavelength. At these frequencies the substrates are able to sustain substrate-modes. In substrate supported transmission lines one would expect substrate-mode losses because the phase velocities of the modes are comparable with the phase velocity of the transmission line resulting in power coupling into these extraneous modes. For certain lines these losses can be prohibitively high. This is an interesting problem because of its similarities with the leaky wave phenomena. Oliner [18] has studied the leaky properties extensively. Practical microstrip lines use very thin substrates compared to their line width. Therefore one does not expect to have substantial substrate-mode losses in microstrip lines. In this chapter, the substrate-mode losses of coplanar strips and coplanar slots (Fig. 2.1) are investigated. A comparative study of dielectric absorption losses and conductor losses is also given.

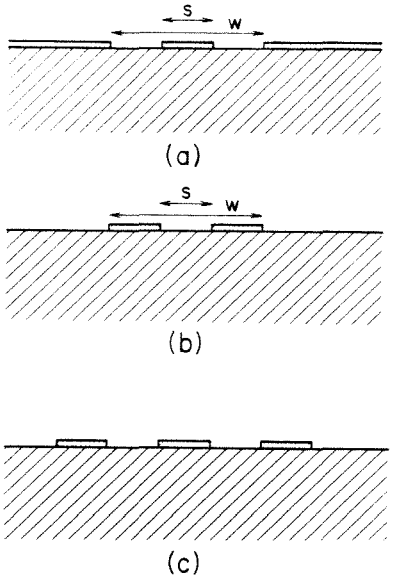

Figure 2.1 Coplanar transmission lines - (a) Coplanar waveguide (b) two-strip line (c) three-strip line.

The propagation properties of the lines are required to predict the substrate-mode losses. The propagation constant and the characteristic impedance of the lines may be obtained through analytical approximations [7] or numerical methods [5,6,9]. For most calculations the quasi-static approximations are sufficient. But for more accurate results one has to use numerical methods. In the next section I review the work on the calculation of the propagation properties of coplanar transmission lines. This is followed by the section on substrate-mode losses. The chapter concludes with the section on other forms of losses.

2.1 Phase Constants for Coplanar Transmission Lines

The study of microstrip lines has been going on since the late sixties. Various numerical methods have been used to predict the propagation constant (also phase velocity) and the characteristic impedance of microstrip lines [5–7]. A comparable amount of work has been done on predicting the propagation prop-

erties of coplanar transmission lines [7–12]. In this section some of the numerical calculations for the propagation properties of coplanar transmission lines are reviewed. The analysis is based on Knorr and Kuchler's method [9].

Their analysis is very similar to the analysis of microstrip lines by Itoh and Mittra [6]. This method is a hybrid-mode analysis, which assumes the fields are a linear combination of TE and TM modes. The presence of the strips does not allow a pure TE or TM mode to exist. Instead a linear combination of these modes is allowed when the dielectric material is isotropic. This is assumed to be true for the materials in this work.

The TE and TM modes are expressed in terms of scalar potentials in both air and the dielectric. The components are then Fourier transformed in the direction parallel to the air-dielectric boundary. Matching the boundary conditions gives a set of coupled equations relating the currents on the strips to the fields at the air-dielectric boundary through appropriate Green's functions. These equations may also be derived by the immitance matrix approach of Itoh and Menzel [19]. The latter method gives a better insight into the physics at the boundary. The coupled equations are solved by the Galerkin method to give values for the line propagation constant at different frequencies. The losses may also be calculated by using the appropriate modifications.

Fig. 2.2 shows the effective dielectric constants of a coplanar waveguide, a two-strip line and a three-strip line. The effective dielectric constants of the coplanar waveguide and the two-strip line are very similar to that of the slot line [10]. When the thickness is small compared to the wavelength the propagation constant tends towards the quasi-static value. The quasi-static value is the propagation constant in a medium of mean dielectric constant given by

$$\bar{\epsilon} = \frac{\epsilon + 1}{2} \tag{2.1}$$

As the thickness is increased with respect to the wavelength, the effective dielectric constant tends towards that of the substrate. This is because at higher frequencies the modes are better confined and most of the power is carried in the dielectric.

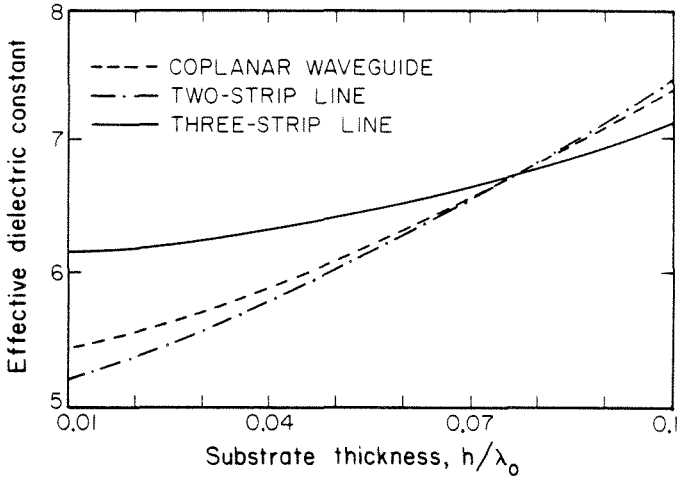

Figure 2.2 Effective dielectric constants of a coplanar waveguide, a two-strip line and a three-strip line on silicon substrates which are assumed to be lossless. This calculation was done using the immitance matrix method.

Another important observation is that when the thickness of the substrate is increased (or when the frequency is increased) the line excites substrate-modes in the dielectric. This is reflected by the poles in the complex plane of the Green's function. The power coupled into the substrate-modes may be obtained from the residues of these poles [20–21]. But this calculation is laborious, as it involves contour integration. In the next section the substrate-mode power is calculated using a much simpler reciprocity argument.

The three-strip transmission line has not been analyzed before. This line was analyzed using a method similar to Knorr and Kuchler's. The line was found to be a lot less dispersive than the two-strip line. The reasoning here being

that the three-strip line forms a quadrapole resulting in better confinement of the energy within the substrate. While the two-strip line forms a dipole which is more sensitive to the thickness of the substrate. The power coupled into substrate-modes is greater for a dipole than a quadrapole, because the quadrapole moment is smaller than the dipole moment for small line separations. This effect makes the substrate-mode losses of the three-strip line a lot smaller than the two-strip line. These two factors make the three-strip line a much more attractive proposition than the two-strip line in integrated circuits where a microstrip line might be difficult to fabricate.

The characteristic impedance is obtained by calculating the total power transmitted by the line. By integrating the Poynting vector over a cross section of the line one gets the total power. A simpler method would be to assume a TEM-like expression in terms of the dispersive properties as shown by Denlinger [5]. Approximate analytical expressions for the characteristic impedance are given in Gupta *et al* [7]. The quasi-static approximation for the characteristic impedance of a two strip line is

$$Z_0 = \eta_m \frac{K(k)}{K'(k)} \tag{2.2}$$

where η_m is the wave impedance in a medium of dielectric constant $\bar{\epsilon}$. $K(k)$ and $K'(k)$ are elliptic integrals [22] and k is the geometric factor defined by Gupta *et al*. Similarly the quasi-static value of the characteristic impedance of a coplanar waveguide is given by

$$Z_0 = \frac{\eta_m}{4} \frac{K'(k)}{K(k)} \tag{2.3}$$

2.2 Substrate-Mode Losses in Coplanar Transmission Lines

Dielectric substrates whose thickness is comparable with the wavelength in that medium may sustain substrate-modes [23-24]. This concept is utilized in

dielectric waveguides and leaky wave antennas [18,25]. This waveguiding property (Fig. 2.3) of substrates manifests as a loss in integrated circuit transmission lines. It may also increase the cross talk between various elements in the circuit. In the case of antennas on thin substrates, this results in a loss in gain. Alexopoulos and co-workers [20,21,26] have investigated the latter aspect. Goubau [27] had investigated the excitation of substrate-modes by elementary sources as early as 1952. He showed that the total field can be represented by a linear combination of substrate-modes and a supplementary field. The substrate-mode losses in coplanar transmission lines are investigated in this section.

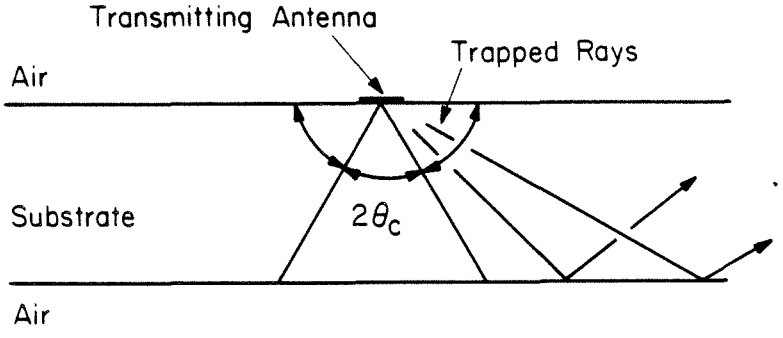

Figure 2.3 Transmitting antenna on a dielectric substrate showing rays trapped as substrate-modes.

Determining the substrate-mode fields is a laborious calculation of the residues of the poles of a Sommerfeld integral [28–30]. This procedure is only necessary when the fields are required, such as in the impedance calculations of microstrip dipoles [20] and in the power calculations of lossy substrates [31]. However, the far-fields within substrate, can be found by reciprocity. On lossless substrates, the far-field can be integrated to find the total power. This method is discussed for line sources by Walter [32] and more recently for elementary sources by Alexopoulos *et al* [26]. The advantage of the reciprocity calculation is that it is much

simpler and it also shows the physical factors that influence the substrate mode power in each mode. For instance, it will be shown that the substrate-mode power is inversely proportional to the quantity h_e, which is the effective guide thickness. Physically this means that when the mode is well confined, the substrate-mode losses are high. The Lorentz reciprocity theorem as given by Harrington [33] is as follows

$$\int_S (\mathbf{E_1} \times \mathbf{H_2} - \mathbf{E_2} \times \mathbf{H_1}) \cdot \mathbf{dS} = \int_V (\mathbf{E_1} \cdot \mathbf{J_2} - \mathbf{E_2} \cdot \mathbf{J_1})\, dV \tag{2.4}$$

where subscripts 1 and 2 refer to fields and currents associated with sources 1 and 2 respectively. In the next section this equation is used to find the substrate-mode fields in different types of coplanar transmission lines.

For a transmission line to sustain substrate-modes the propagation constant of the substrate-modes along the line has to be equal to the line propagation constant. Therefore the substrate-modes will propagate at an angle ψ, where

$$\cos\psi = k_z/\beta \tag{2.5}$$

and k_z is the line propagation constant, β the propagation constant of the substrate-mode. Fig. 2.4 shows the measured substrate-mode radiation patterns for a two-strip line on a substrate of dielectric constant 12.

Clearly for any given mode, β has to be greater than k_z, for it to be excited by the transmission line. This is the reason why in the previous section the calculation of propagation constants of coplanar transmission lines was reviewed. Fig. 2.5 shows the dispersion curves for substrate-modes as a function of thickness for a substrate of dielectric constant 12. The full lines are the dispersion curves of ungrounded substrates while the broken lines are those of parallel plate waveguides. Parallel plate guides have metallic planes on both surfaces of the substrate while a grounded substrate has a metallic plane on only one surface.

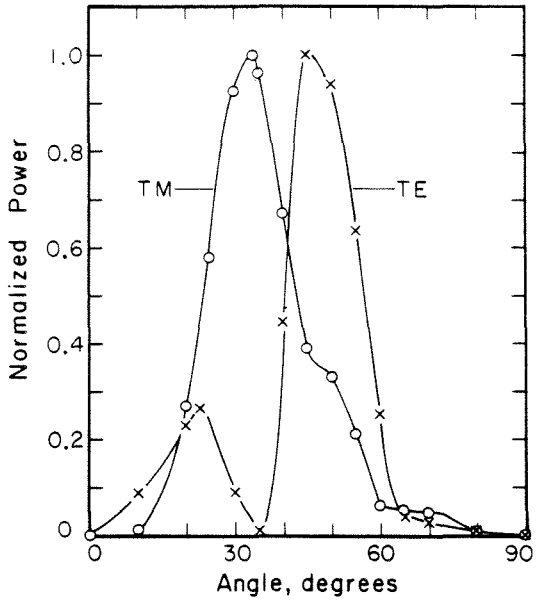

Figure 2.4 Measured substrate-mode radiation pattern from a two-strip line on a substrate ($\epsilon = 12, h = 1.2$cm) at 5 GHz. The angles ψ_{TM} and ψ_{TE} are 21° and 37° respectively.

Also shown in this plot is the quasi-static propagation constant, k_m. As β has to be greater than k_z for a certain mode to be excited it is clear from the figure that each mode except the TEM mode will have a cutoff thickness below which the mode won't be excited by a particular line. Although the quasi-static value for the line propagation constant is used here for more accurate predictions of the cutoff thickness, one has to use the frequency dependent value calculated in the previous section. For the ungrounded substrate the first mode that drains away energy is the TE_0 mode. For the grounded substrate, like in a microstrip line the first losses are due to the TM_0 mode and for a parallel plate guide they are due to both TE_1 and TM_1 modes. Only a parallel plate guide may have losses due to the TEM mode. Fig. 2.6 shows a mode plot for ungrounded substrates, grounded substrates and parallel plate waveguide.

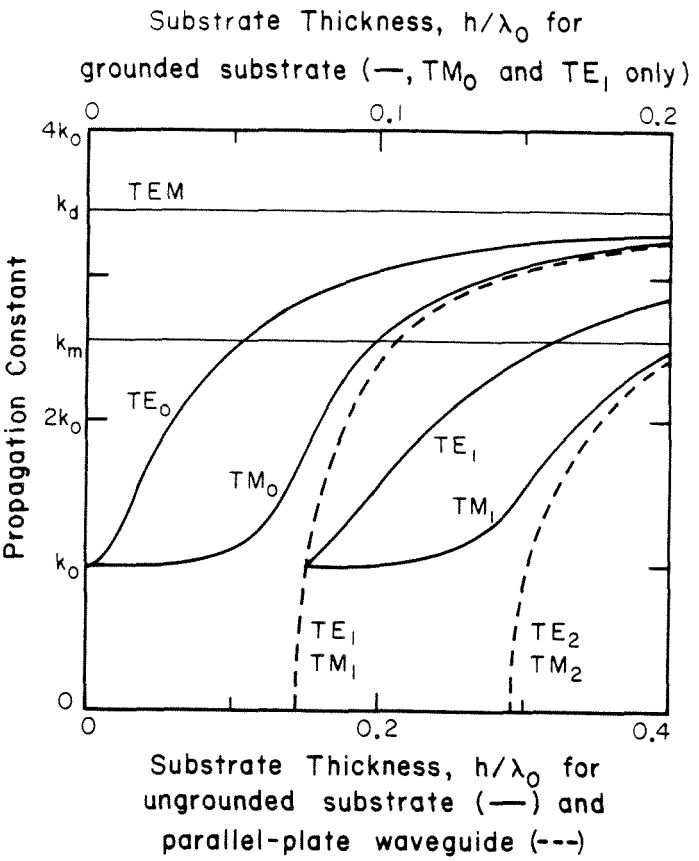

Figure 2.5 Dispersion curves for substrate-modes in ungrounded, grounded and parallel plate substrates, as a function of thickness, with $\epsilon = 12$.

The substrate-mode calculations using reciprocity are relatively straight forward. Fig. 2.8 shows the magnetic source $\mathbf{M_1}$ at $x = x_0$ producing a TM substrate field with transverse components $\mathbf{E_1}$ and $\mathbf{H_1}$ at $x = 0$. For reciprocity consider a second substrate-mode field, $\mathbf{E_2}$, $\mathbf{H_2}$ originating outside the box and propagating in the opposite direction. Applying equation (2.4) to a large box S, only the right hand side of the box contributes to the surface integral since the modes exactly cancel at the left hand side, one gets

$$\mathbf{M_1}.\mathbf{H_2}\, dl = 2\mathbf{E_1}\mathbf{H_2}\, dl h_e \tag{2.6}$$

where h_e is the effective height.

The effective height is the actual thickness plus the apparent ray penetration depth z_o, (Fig. 2.8) required by the Goos-Hanschen shift [23], $2x_o$, on each side

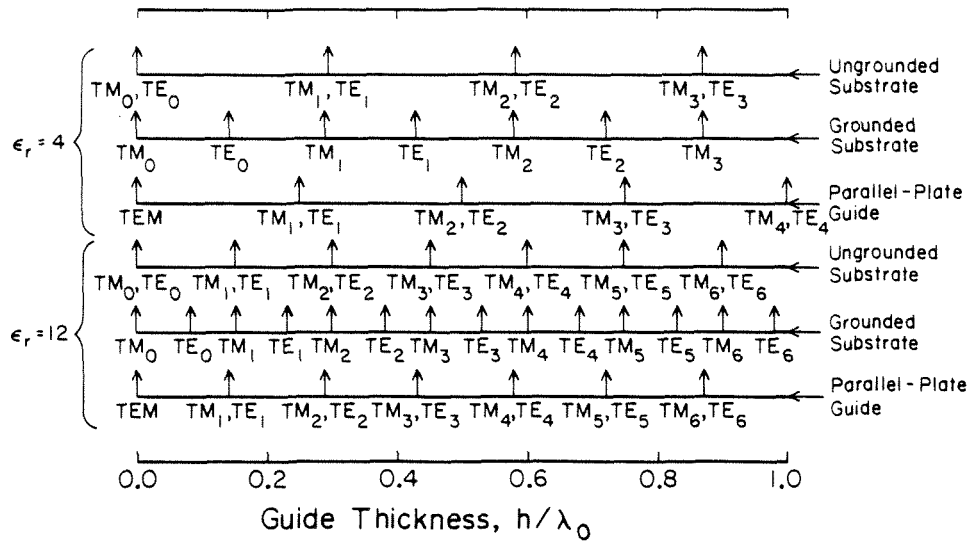

Figure 2.6 Propagating modes for ungrounded, grounded and parallel plate substrates for $\epsilon = 4$ and 12.

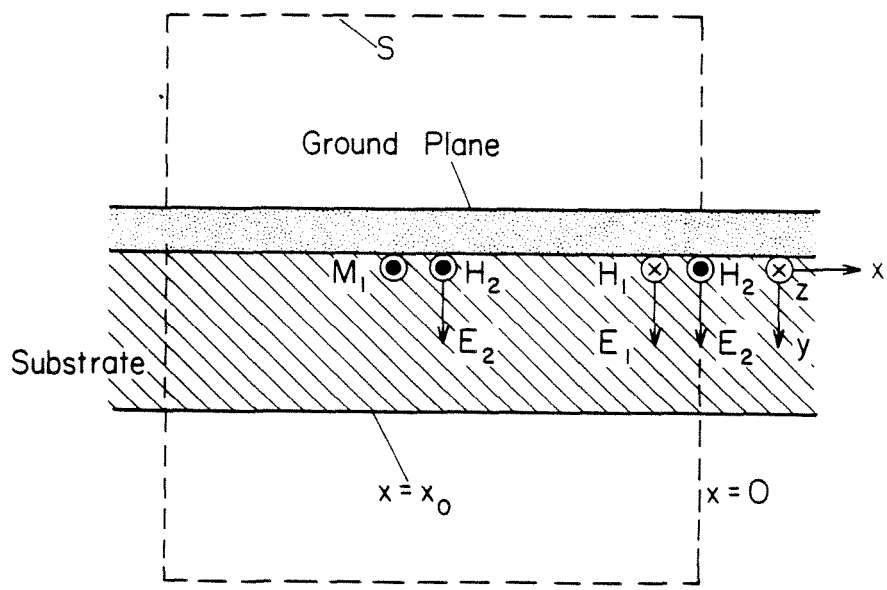

Figure 2.7 Reciprocity calculation for a slot on grounded plane.

of the substrate. For TE modes, z_o is

$$z_o = 1/\alpha \tag{2.7}$$

Here α is the evanescent constant in air, given by

$$\alpha = \sqrt{\beta^2 - k_0^2} \tag{2.8}$$

where β is the guide propagation constant. For TM modes, z_o is given by

$$z_o = \frac{1}{\alpha}\left[\frac{\beta^2}{k_d^2} + \frac{\beta^2}{k_0^2} - 1\right]^{-1} \tag{2.9}$$

For slabs without ground plane the effective height is

$$h_e = h + 2z_o, \tag{2.10}$$

where h is the actual substrate thickness. For slabs with a ground plane the effective height is

$$h_e = h + z_o \tag{2.11}$$

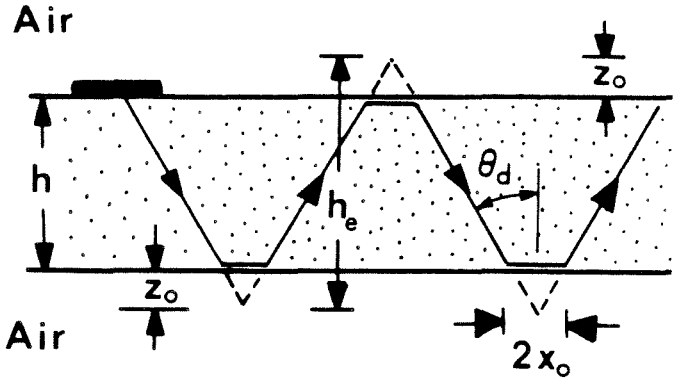

Figure 2.8 Ray optics picture of dielectric waveguide propagation (Kogelnik [23]).

The advantage of using the effective thickness is that one can relate h_e to the power per unit width P, in all these modes given by the formula

$$P = \frac{EHh_e}{4} \tag{2.12}$$

In calculating the substrate-mode losses it will be seen that the losses are inversely proportional to h_e.

One may find the power in the substrate-modes by invoking the reciprocity equation, (2.4). Details of the calculations are given in [1]. The power lost per

unit length to TM modes, P_{TM}, from a slot line carrying a voltage $V exp(-k_z z)$ is given by

$$P_{TM} = \frac{V^2}{2\eta_d h_e} \frac{\sin\psi}{\sin\theta_d} \tag{2.13}$$

where η_d is the characteristic impedance of the dielectric and θ_d the angle of incidence in the substrate (Fig. 2.8). Similarly the power lost to TE modes is given by

$$P_{TE} = \frac{V^2}{2\eta_d h_e} \frac{\sin\psi}{\sin\theta_d} \frac{\cos\theta_d}{\tan\psi} \tag{2.14}$$

In calculating the above formulas it was assumed that the slot width was very small compared to a wavelength.

Again omitting the details, one may derive the substrate-mode attenuation coefficient of a coplanar waveguide from equations (2.13) and (2.14). Assuming quasi-static approximations for the impedance and the field distributions the substrate-mode attenuation coefficient for TM modes, for a coplanar waveguide may be written as

$$\alpha_{TM} = \frac{\pi^2}{8} \sqrt{\frac{2\epsilon_r}{\epsilon_r + 1}} \frac{\sin^3\psi \sin\theta_d}{h_e K(k) K'(k)} \left(\frac{w}{\lambda_d}\right)^2 \tag{2.15}$$

The attenuation coefficient for TE modes α_{TE} is given by

$$\alpha_{TE} = \frac{\pi^2}{8} \sqrt{\frac{2\epsilon_r}{\epsilon_r + 1}} \frac{\sin\psi \cos^2\psi \sin\theta_d \cos^2\theta_d}{h_e K(k) K'(k)} \left(\frac{w}{\lambda_d}\right)^2 \tag{2.16}$$

The corresponding losses for a single strip line on a dielectric substrate may also be obtained from the reciprocity equation. The losses due to the TE modes are

$$P_{TE} = \frac{I^2 \eta_d}{2h_e} \frac{\sin\psi}{\sin\theta_d} \cos^2\phi_{TE} \tag{2.17}$$

where ϕ_{TE} is given by Kogelnik. The TM losses are

$$P_{TM} = \frac{I^2 \eta_d}{2h_e} \frac{\sin\psi}{\sin\theta_d} \sin^2\phi_{TM} \frac{\cos^2\theta_d}{\tan^2\psi} \tag{2.18}$$

Again assuming the quasi-static approximation for the impedance and the field distributions the TE mode attenuation coefficient for a two-strip line is

$$\alpha_{TE} = \frac{\pi^4}{2\sqrt{2}} \sqrt{\frac{\epsilon_r + 1}{\epsilon_r}} \frac{\sin^3 \psi \sin \theta_d}{h_e K(k) K'(k)} \cos^2 \phi_{TE} \left(\frac{w}{\lambda_d} \right)^2 \tag{2.19}$$

and the TM mode attenuation coefficient is

$$\alpha_{TM} = \frac{\pi^4}{2\sqrt{2}} \sqrt{\frac{\epsilon_r + 1}{\epsilon_r}} \sin \psi \cos^2 \psi \sin \theta_d \cos^2 \theta_d \sin^2 \phi_{TM} \left(\frac{w}{\lambda_d} \right)^2 \tag{2.20}$$

These expressions for the losses were also derived in [1].

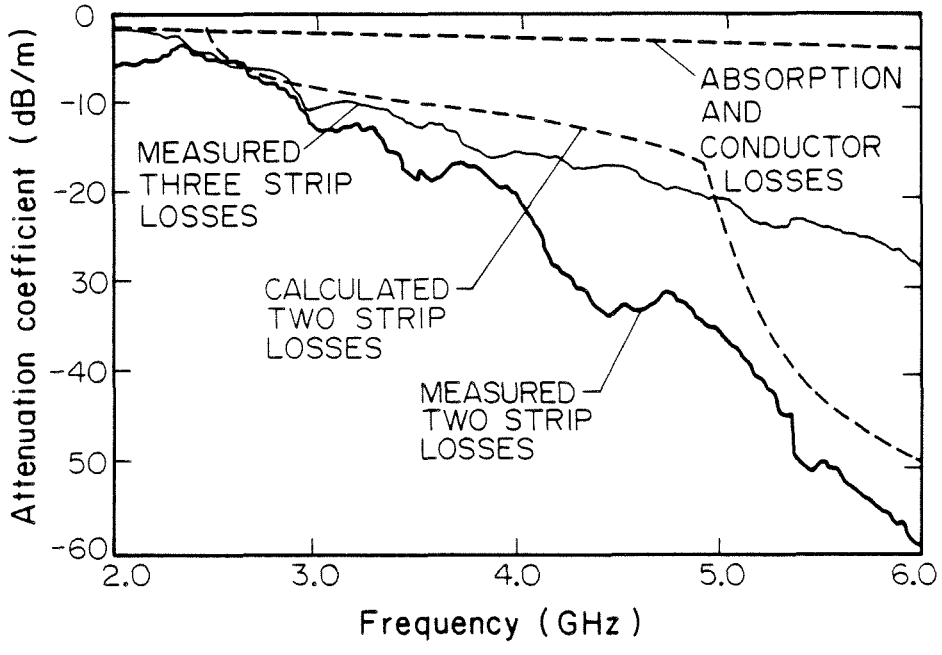

Figure 2.9 The substrate-mode losses of a two-strip line and a three-strip line on a silicon substrate with $w = 2\text{mm}, s = 1\text{mm}, h = 2.5\text{cm}$. Also shown are the dielectric absorption losses and the conductor losses of the two-strip line.

Fig. 2.9 shows the substrate-mode attenuation coefficient of a two-strip line plotted as a function of frequency. Also shown are the losses measured in the millimeter-wave integrated circuit laboratory. These losses were measured for a 6-inch line on a Stycast substrate of dielectric constant 12. At low frequencies

the substrate-mode losses are non existent. But as the frequency is increased the modes turn on one by one. This is shown by the sudden changes in the slope of the calculated curve.

The measured substrate-mode losses of a three-strip line are also shown in Fig. 2.9. These losses are considerably smaller than the corresponding losses of the two-strip line. As shown in equations 2.19 and 2.20, the power lost to substrate-modes in a two-strip line is proportional to the square of the line width. This means that the losses are proportional to the dipole moment. But in a three-strip line one has a quadrapole, which means the losses will be smaller than those due to a dipole. Although an analytical expression for the substrate-mode losses of a three-strip line is not easy to obtain it is fair to assume that these losses are proportional to the fourth power of the line width.

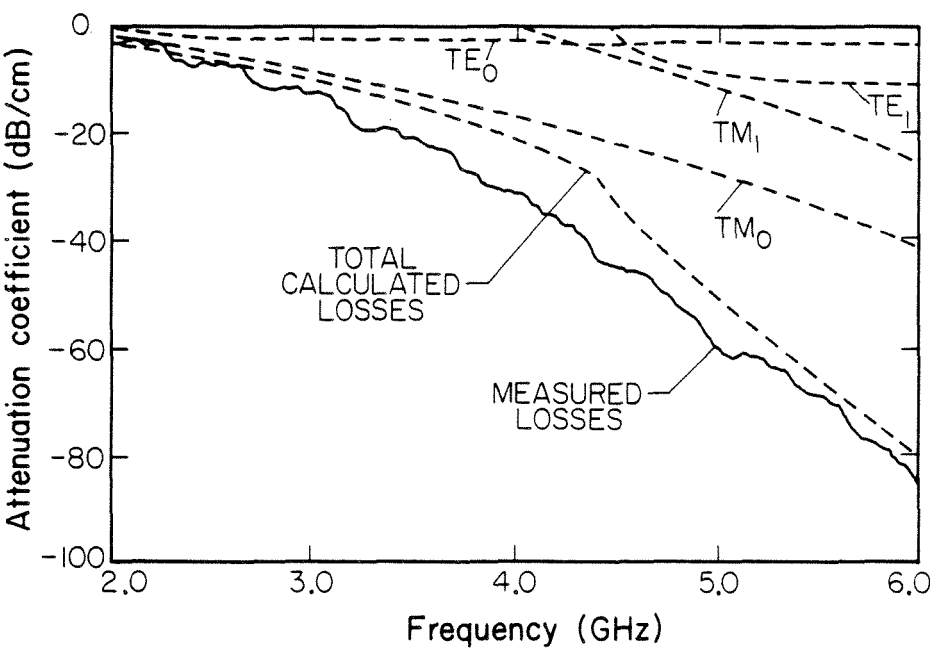

Figure 2.10 The substrate-mode losses of a coplanar waveguide on a silicon substrate with $w = 2\text{mm}, s = 1\text{mm}, h = 2.5\text{cm}$. Also shown are the losses of each individual mode.

Fig. 2.10 shows the substrate-mode losses of a coplanar waveguide. Also

shown are the losses measured in the integrated circuits laboratory. The presence of the ground plane makes the TM_0 mode turn on first. In the coplanar waveguide the coupling is greater into the TM modes than the TE modes. It can be shown that the substrate-mode losses due to the TE modes tend to zero when the frequency is increased while the losses due to TM modes are proportional to the square of the frequency. This also holds true for the losses of a two-strip line.

Several different methods have been tried to control the substrate modes. Clifton *et al.* [1] achieved very good results at 110 GHz by mounting the substrate at the end of a hollow metal waveguide. Inside the waveguide, the substrate-modes can be excited only near their resonant frequencies. By operating away from these resonances one is able to minimize the losses. Another method is to keep the width of the current carrying elements small. The design width will have to be a compromise between substrate-mode losses that increase for large lines, and conductor losses which increase for small lines.

2.3 Dielectric Absorption Losses and Conductor Losses in Coplanar Transmission Lines

Pucel [13] investigated the dielectric absorption losses and the conductor losses of microstrip lines. The dielectric loss and the conductor loss are proportional to the loss tangent and the sheet resistance, respectively. The conductor loss is also inversely proportional to the width of the current element. Other investigators have found similar relationships for the absorption losses and conductor losses of coplanar transmission lines [14–17]. The absorption losses and the conductor losses of a two-strip line are shown in Fig 2.9. These losses were calculated using expressions from Gopinath [17]. This figure clearly illustrates why it is important that substrate-modes be suppressed.

2.4 Conclusion

When the substrate thickness is comparable with the free space wavelength, coplanar transmission lines couple power into substrate-modes. These substrate-mode losses are considerably higher than the dielectric absorption losses and the conductor losses and are prohibitively large at millimeter-wave frequencies. The substrate-mode losses of a three-strip line are smaller than the losses of either a two-strip line or a coplanar waveguide. Furthermore the three-strip line is less dispersive than the latter two. The substrate-mode losses of practical microstrip lines are considerably smaller.

References.

[1] D. B. Rutledge, D. P. Neikirk, D. P. Kasilingam, **"Integrated Circuit Antennas,"** *Infrared and Millimeter Waves*, **10**, pp. 1–90, K. J. Button, ed., Academic Press, Inc., New York, 1983.

[2] B. J. Clifton *et al.*, "High Performance Quasi-Optical GaAs Monolithic Mixer at 110 GHz.," *IEEE Trans. Electron Devices*, **ED-28**, pp. 155–157, 1981.

[3] N. L. Wang, S. E. Schwarz, "Planar Oscillators for Monolithic Integration," *Intl. J. of Infrared and Millimeter Waves*, **3**, pp. 771–782, 1982.

[4] D. F. Williams, S. E. Schwarz, "Design and Performance of Coplanar Waveguide Bandpass Filters," *IEEE Trans. Microwave Theory Tech.*, **MTT-31**, pp. 558–566, 1983.

[5] E. J. Denlinger, "A Frequency Dependent Solution for Microstrip Transmission Lines," *IEEE Trans. Microwave Theory Tech.*, **MTT-19**, pp. 30–39, 1971.

[6] T. Itoh, R. Mittra, "Spectral-Domain Approach for Calculating the Dispersion Characteristics of Microstrip Lines," *IEEE Trans. Microwave Theory Tech.*, **MTT-21**, pp. 496–499, 1973.

[7] K. C. Gupta *et al.*, *Microstrip Lines and Slotlines*, Artech House, Inc., Dedham, MA. 1979.

[8] S. B. Cohn, "Slot Line on a Dielectric Substrate," *IEEE Trans. Microwave Theory Tech.*, **MTT-17**, pp. 768–778, 1969.

[9] J. B. Knorr, K. D. Kuchler, "Analysis of Coupled Slots and Coplanar Strips on Dielectric Substrates," *IEEE Trans. Microwave Theory Tech.*, **MTT-23**, pp. 541–548, 1975.

[10] T. Itoh, R. Mittra, "Dispersion Charateristics of Slot LInes," *Electron. Lett.*, **7**, pp. 364–365, 1975.

[11] C. P. Wen, "Coplanar Waveguide: A Surface Strip Transmission Line Suitable for Nonreciprocal Gyromagnetic Device Applications," *IEEE Trans. Microwave Theory Tech.*, **MTT-17**, pp. 1087–1090, 1969.

[12] R. Pregla, S. G. Pintzos, "Determination of the Propagation Constants in Coupled Microslots by a Variational Method," *Proc. V Colloquium Microwave Comm.*, Budapest, pp. MT 491–500, 1974.

[13] R. A. Pucel *et al.*, "Losses in Microstrip," *IEEE Trans. Microwave Theory Tech.*, **MTT-16**, pp. 342–350, 1968.

[14] M. V. Schneider, "Dielectric Loss in Integrated Microwave Circuits," *BSTJ*, **48**, pp. 2325–2332, 1969.

[15] R. Pregla, "Determination of Conductor Losses in Planar Waveguide Structures," *IEEE Trans. Microwave Theory Tech.*, **MTT-28**, pp. 433–434, 1980.

[16] J. D. Welsh, H. J. Pratt, "Losses in Microwave Transmission Systems for Integrated Microwave Circuits," *NEREM Rec.*, **8**, pp. 100–101, 1966.

[17] A. Gopinath, "Losses in Coplanar Waveguides," *IEEE Trans. Microwave Theory Tech.*, **MTT-30**, pp. 1101–1104, 1982.

[18] A. A. Oliner *et al.*, "Guidance and Leakage Properties of a Class of Open Dielectric Waveguides: Part 11 – New Physical Effects," *IEEE Trans. Microwave Theory Tech.*, **MTT-29**, pp. 855–869, 1981.

[19] T. Itoh, W. Menzel, "A Full-Wave Analysis Method for Open Micostrip Structures," *IEEE Trans. Antenna Propagat.*, **AP-29**, pp. 63–67, 1981.

[20] N. G. Alexopoulos, I. E. Rana, "Mutual Impedance Computation between Printed Dipoles," *IEEE Trans. Antenna Propagat.*, **AP-29**, pp. 106–111, 1981.

[21] I. E. Rana, N. G. Alexopoulos, "Current Distribution and Input Impedance of Printed Dipoles," *IEEE Trans. Antennas Propagat.*, **AP-29**, pp. 99–105,

1981.

[22] M. Abramowitz, I. A. Stegun, *A Handbook of Mathematical Functions*, Dover Publications, New York, 1964.

[23] H. Kogelnik, *Integrated Optics*, T. Tamir, ed., Springer-Verlag, New York, 1975.

[24] A. Yariv, *Quantum Electronics*, pp. 508–544, J. Wiley, New York, 1975.

[25] R. Chatterjee, *Dielectric and Dielectric Loaded Antennas*, Research Studies Press, Letchworth, England, 1985.

[26] N. G. Alexopoulos *et al.*, "Substrate Optimization for Integrated Circuit Antennas," *IEEE Trans. Microwave Theory Tech.*, **MTT-31**, pp. 550–557, 1983.

[27] G. Goubau, "On the Excitation of Surface Waves," *Proc. IRE*, pp. 865–868, 1952.

[28] R. E. Collin, *Field Theory of Guided Waves*, McGraw-Hill, New York, 1960.

[29] L. B. Felsen, N. Marcuvitz, *Radiation and Scattering of Waves*, Prentice-Hall, New York, 1973.

[30] H. M. Barlow, J. Brown, *Radio Surface Waves*, Oxford University Press, Oxford, 1962.

[31] R. R. Chance *et al.*, *Adv. in Chemical Physics*, **37**, pp. 1–65, 1978.

[32] C. H. Walter, *Traveling Wave Antennas*, McGraw-Hill, New York, 1965.

[33] R. F. Harrington, *Time Harmonic Electromagnetic Waves*, McGraw-Hill, New York, 1961.

[34] M. N. Afsar, "Dielectric Measurements of Millimeter-Wave Materials," *IEEE Trans. Microwave Theory Tech.*, **MTT-32**, pp. 1598–1609, 1984.

CHAPTER 3

Radiation Losses of Transmission Lines on Thick Dielectric Substrates

A variety of coplanar metal structures have been used to guide waves on thick dielectric substrates [1–2]. As mentioned in the previous chapter, coplanar waveguides, coplanar strip lines, and three-strip lines are some of them. Another common transmission line, the slot line, has radiation losses on a thick substrate that are too large to be useful. Unlike transmission lines on thin substrates which tend to couple power into substrate-modes, lines on thick substrates tend to radiate power directly into the dielectric. The radiation occurs because the wave velocity of the transmission line is greater than the phase velocity of the waves in the dielectric. The radiation is similar to that of a leaky-wave antenna [3–4] and is emitted in a semi-cone (Fig. 3.1) near an angle ψ given by

$$\cos\psi = k_z/k_d \tag{3.1}$$

where k_z is the guide propagation constant and k_d is the propagation constant in the dielectric. These losses have to be controlled if these lines are to be used either as guides or as antennas. In this chapter, the radiation losses of transmission lines on thick substrates are investigated.

Dispersion characteristics of transmission lines on thick substrates may be calculated in a manner similar to those of lines on thin substrates [5–6]. The Green's functions are different for thick substrates and the calculations involve complex integration. Compton *et al.* [7], Pozar [8], Kominami *et al.* [9] have investigated the radiation properties of antennas on dielectric half spaces. The radiation was found to be primarily into the dielectric. This is because the phase velocity in the dielectric is lower than the phase velocity in air. This results in radiation from a fast-wave structure into the substrate.

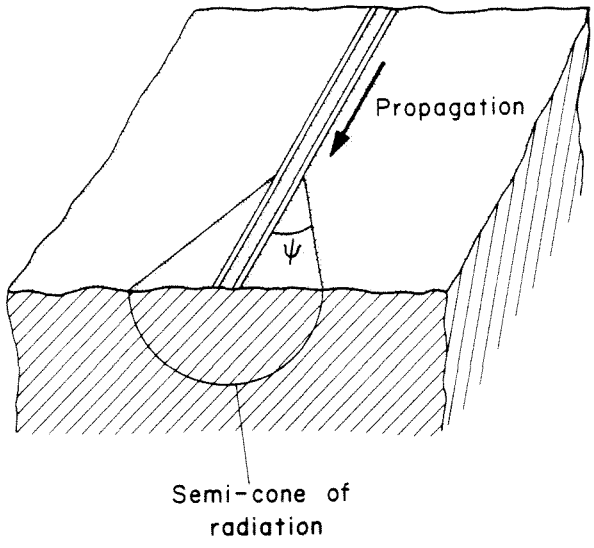

Figure 3.1 Radiation from a two-slot line on a thick substrate, showing a semicone of radiation near an angle $\psi = \cos^{-1}(k_x/k_d)$.

3.1 Antennas on Thick Substrates

In the previous chapter it was shown that antennas and transmission lines on dielectric substrates couple power into substrate-modes. To prevent power being coupled into these extraneous modes, Brewitt-Taylor *et al.* [10] and Neikirk *et al.* [11] mounted a lens with the same dielectric constant on the back side of the substrate. This eliminates the substrate-mode problem because radiation incident on the lens surface does not suffer total internal reflection and except for a small reflected wave, propagates right through this surface. This reflected power may be minimized by using quarter-wave matching layers [12–13]. This gave rise to the substrate-lens coupled system. Fig. 3.2 shows two commonly used substrate lenses, the hemispheric lens and the hyperhemispheric lens. Antennas and transmission lines in lens coupled systems behave similar to systems on dielectric half-spaces.

Performance of elementary sources on dielectric half-spaces has been given in Rutledge *et al.* [1]. Elementary slots were shown to radiate power into the

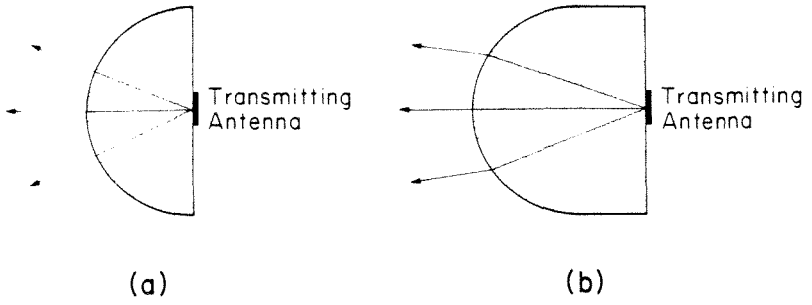

Figure 3.2 Substrate lenses - (a) the hemispheric lens and (b) the hyperhemispheric lens.

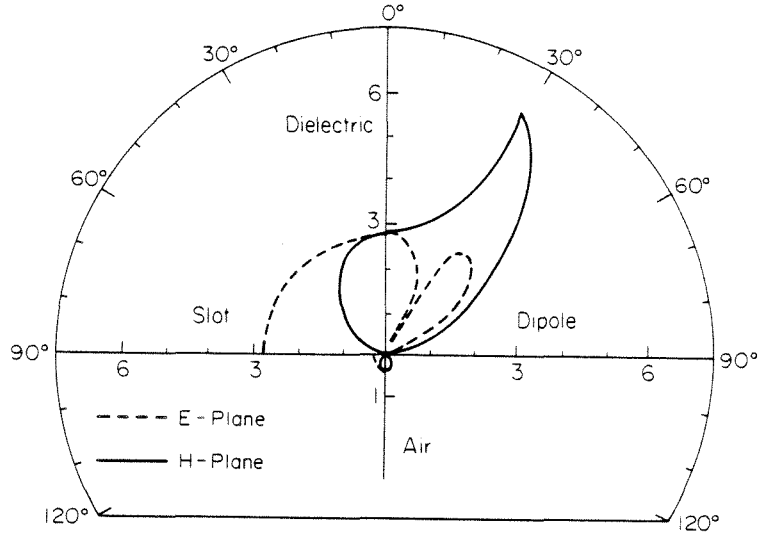

Figure 3.3 The radiation pattern of a slot and a dipole on quartz half-space ($\epsilon = 4$ from Rutledge *et al.*).

two half-spaces in the ratio $\epsilon^{3/2} : 1$, where ϵ is the dielectric constant of the substrate. The situation is a little more complicated in the case of elementary dipoles. But for large dielectric constants the radiated power in the dielectric dominates the power in the air by roughly the same factor as in slots. Fig. 3.3 shows the radiation pattern of dipoles and slots on dielectric half-spaces. In the next section the radiation properties of transmission lines are investigated. The reciprocity relationship is used to calculate the radiation losses of two-strip lines and two-slot lines.

3.2 Radiation Losses of Coplanar Transmission Lines

The radiation losses may be calculated using reciprocity. The power radiated by a travelling wave magnetic line current on a ground plane is calculated first because this approach allows one to extend the calculations to coplanar waveguides. A rigorous solution of Maxwell's equations [14] will yield similar results in the far field. Omitting the details it can be shown [1] that the radiated power P_r is given by

$$P_l = \frac{\omega \epsilon_d V^2 \sin^2 \psi}{16\pi} \int_{-\pi/2}^{\pi/2} 4 d\phi \tag{3.2}$$

Similarly the power radiated by a line current on a thick dielectric substrate is given by

$$P_l = \frac{\omega \mu_0 I^2 \sin^2 \psi}{16\pi} \int_{-\pi/2}^{\pi/2} \tau^2 d\phi \tag{3.3}$$

where τ is given by

$$\tau = \frac{\tau_{TM} \cos^2 \psi + \tau_{TE} \tan^2 \phi}{\cos^2 \psi + \tan^2 \phi} \tag{3.4}$$

τ is also proportional to the radiation pattern of the transmission line. Fig. 3.4 shows the radiation pattern of two-slots and two-strips in the plane normal to direction of propagation..

To apply these formulas to pairs of slots and pairs of strips, one has to integrate across the transmission line. P_l for a two-slot line is given by

$$P_l = \frac{1}{16\pi} k_d^2 \sin^4 \psi \omega \epsilon_d \int_{-\infty}^{+\infty} y E_y dy \int_{-\pi/2}^{\pi/2} 4 \sin^2 \phi d\phi \tag{3.5}$$

where it is assumed that $w k_d \sin \phi < 1$. E_y is the electric field in the slots. The dual expression for the two-strip line is

$$P_l = \frac{1}{16\pi} k_d^2 \sin^4 \psi \omega \mu_0 \int_{-\infty}^{+\infty} y J_z dy \int_{-\pi/2}^{\pi/2} \tau^2 \sin^2 \phi d\phi \tag{3.6}$$

where J_z is the current on the strips. Making the appropriate quasi-static approximations one arrives at the following expressions for the attenuation constants

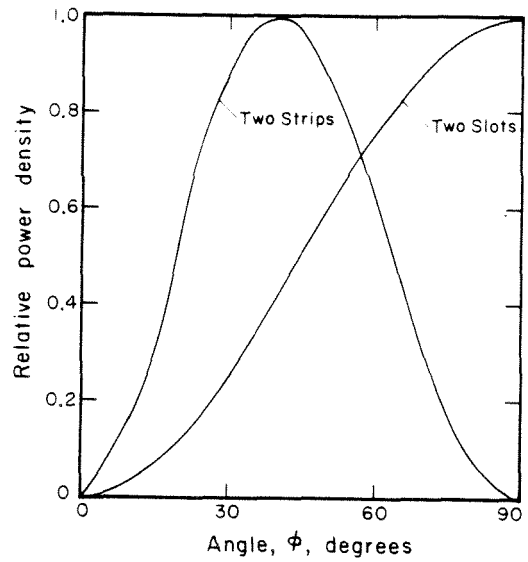

Figure 3.4 Calculated patterns of two-slot and two-strip lines. The curves are normalized to their peak values. The angle ϕ is the angle measured from the normal to the interface.

[1]. The attenuation coefficient of a two-strip line is

$$\alpha = \frac{\pi^5}{32\sqrt{2}} \frac{(1 - 1/\epsilon_r{}^2)}{\sqrt{1 + 1/\epsilon_r}} \frac{w^2}{\lambda_d^3 K(k) K'(k)} \tag{3.7}$$

The attenuation coefficient of a two-slot line is

$$\alpha = \frac{\pi^5 \sqrt{2}}{32} (3 - \sqrt{8}) \sqrt{1 + 1/\epsilon_r} \frac{w^2}{\lambda_d^3 K(k) K'(k)} \tag{3.8}$$

where $K(K)$ and $K'(k)$ are elliptic integrals. k is the geometric factor defined by Gupta *et al.* and ϵ_r the relative dielectric constant of the substrate.

The losses for a three-strip line on a thick substrate can be shown to be proportional to the fourth power of the line width. This makes these losses a lot smaller than the corresponding losses of two-strip lines and two-slot lines. An analytical expression for the losses of the three-strip line is harder to obtain because algebraic simplifications are not available.

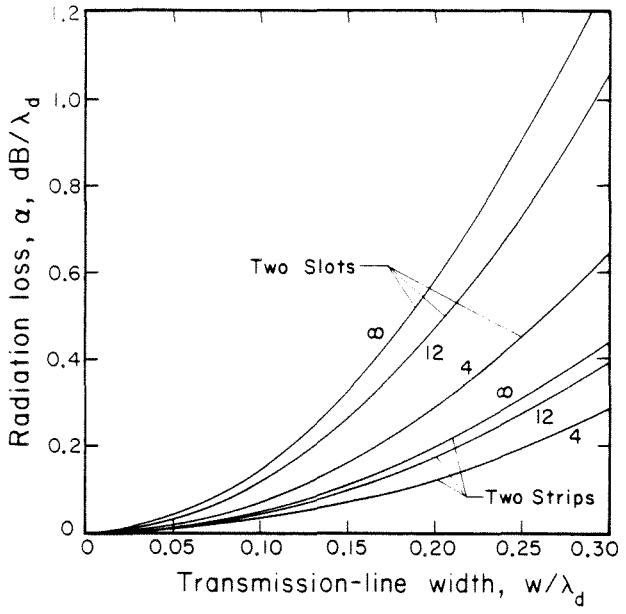

Figure 3.5 Calculated attenuation coefficients for two-slot and two-strip lines.

Fig. 3.5 shows the calculated attenuation coefficients of two-slot lines and two-strip lines for different dielectric constants. As the dielectric constant is increased, the radiation losses increase too. This is because the mismatch in the wave velocities of the line and the dielectric is greater for substrates of high dielectric constant. The losses for two-slot lines are between two and three times as high as those of a two-strip line. In both cases the losses are proportional to the square of the line width. Fig. 3.6 shows the measured radiation losses of a two-slot line on thick substrate of dielectric constant 12. The losses were of the order of 60 dB/m at around 5 GHz which makes it comparable to the substrate-mode losses of a coplanar waveguide from the previous chapter. This is to be expected, because when the frequency is increased, the substrate-mode losses should converge towards the radiation losses of a thick substrate.

There are several ways to control the radiation. The line can be made narrow. But narrow lines have larger conductor losses. Therefore, the design width will have to be chosen so as to compromise between the radiation losses and the

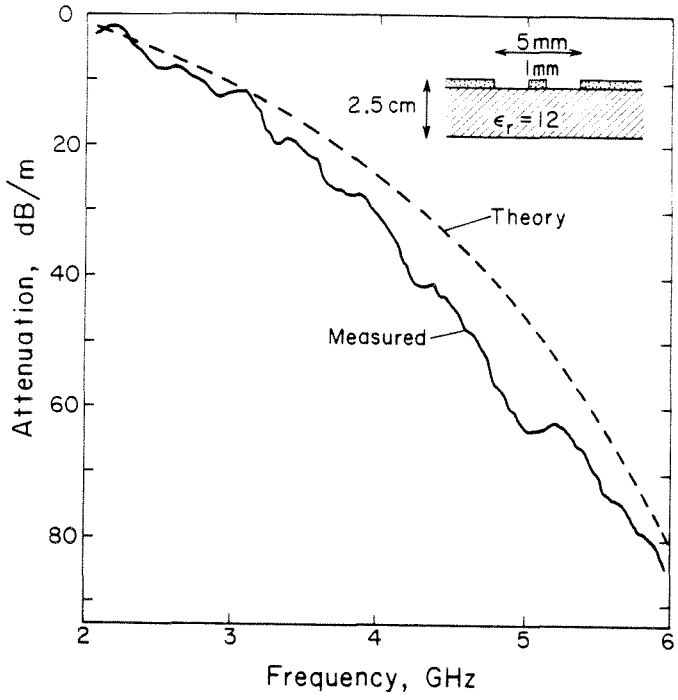

Figure 3.6 Measured radiation losses of a two-slot line on a thick substrate with $\epsilon = 12$.

conductor losses. Another way to reduce the losses is to add a superstrate to form a sandwich line [15]. This slows down the wave velocity of the line thereby reducing the radiation losses.

3.4 Conclusion

The antennas and transmission lines on thick dielectric substrates radiate more into the dielectric than into air. The losses due to this radiation in transmission lines are considerable. These losses are proportional to the line width and may be minimized by using narrow lines. The radiation losses of two-slot lines are almost three times as large as the corresponding losses of a two-strip line. The losses also increase with the dielectric constant of the substrate.

References.

[1] D. B. Rutledge, D. P. Neikirk, D. P. Kasilingam, "Integrated Circuit Antennas," *Infrared and Millimeter Waves*, **10**, pp. 1–90, K. J. Button, ed., Academic Press, Inc., New York, 1983.

[2] K. C. Gupta *et al.*, *Microstrip Lines and Slot Lines*, Artech House Inc., Dedham, MA. 1979.

[3] H. Jasik, *Antenna Engineering Handbook*, McGraw-Hill, New York, 1961.

[4] R. Chatterjee, *Dielectric and Dielectric Loaded Antennas*, Research Studies Press, Letchworth, England, 1985.

[5] T. Itoh, R. Mittra, "Spectral Domain Approach for Calculating the Dispersion Characteristics of Microstrip Lines," *IEEE Trans. Microwave Theory Tech.*, **MTT-21**, pp. 496–499, 1973.

[6] J. B. Knorr, K. D. Kuchler, "Analysis of Coupled Slots and Coplanar Strips on Dielectric Substrates," *IEEE Trans. Microwave Theory Tech.*, **MTT-23**, pp. 541–548, 1975.

[7] R. C. Compton *et al.*, "Bow-Tie Antennas on a Dielectric Half-Space: Theory and Experiment," submitted for publication *IEEE Antennas Propagat.*

[8] D. M. Pozar, "Improved Computational Efficiency for the Moment Method Solution of Printed Dipoles and Patches," *Electromagnetics*, **3**, pp. 299–309, 1983.

[9] M. Kominami *et al.*, "Dipole and Slot Elements and Arrays on Semi-Infinite Substrates," IEEE, **AP-33**, pp. 600–607, June 1985.

[10] C. R. Brewitt-Taylor *et al.*, "Planar Antennas on a Dielectric Surface," *Electon. Lett.*, **12**, pp. 729–731, 1981.

[11] D. P. Neikirk *et al.*, *Proc. SPIE*, **317**, pp. 206–210, 1981.

[12] K. R. Armstrong, F. J. Low, "Far-Infrared Filters Utilizing Small Particle

CHAPTER 4

Focusing Properties of Small Lenses

Substrate lenses are often used in millimeter-wave imaging [1–3] and receiving [4–5] systems to improve the coupling of power into the antennas. Fig. 4.1 shows an imaging system consisting of an objective lens, a hyperhemispheric substrate lens and an imaging antenna array. As shown in the previous chapter, substrate lenses take advantage of the fact that antennas on dielectric substrates are more sensitive to radiation coming from the substrate side [6]. This results in better coupling efficiencies [7]. In addition the substrate lens reduces the size of the image while increasing its intensity [7,8] resulting in an increase in the effective area of the receiving antenna.

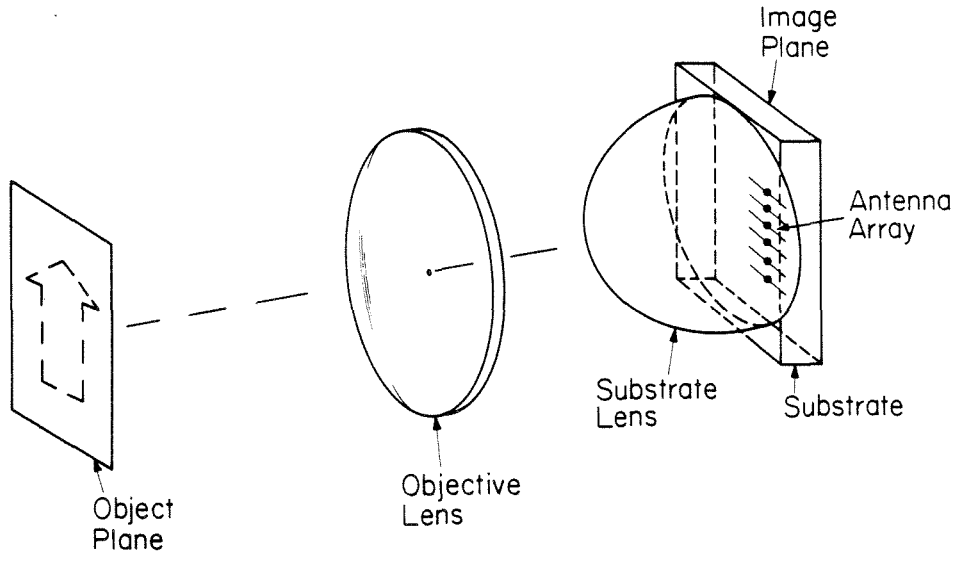

Figure 4.1 Substrate-lens coupled imaging antenna array.

One factor that limits the size of the substrate lens is absorption which can be very high at millimeter-wave frequencies [9]. For example Zah *et al.* [3] estimated the absorption losses of a 2.5 cm diameter hemispherical silicon lens

to be 1 dB at 94 GHz. Another limiting factor is that the antennas must be close together to achieve diffraction limited resolution [1]. This can be a problem for two-dimensional imaging arrays because it is difficult to make low frequency connections in the plane of the array [10].

One approach to these problems is to make a "fly's-eye" array of small lenses with each lens having its own receiving antenna. Fig. 4.2 shows such an imaging system. The idea is that the lenses would increase the apparent effective area of the antenna to about the area of the lens while the physical area of the antenna remains a small fraction of the lens area. For a hyperhemispheric lens, the effective area is increased by a factor of the dielectric constant squared. This means for a silicon lens, the effective area is increased by a factor of about 150. If the lenses can be made small they may be placed close enough to achieve diffraction limited resolution. One also expects the absorption losses to be much smaller than those of a large lens. In this chapter the focusing properties of small lenses are investigated with purpose of finding how small lenses can be made without degrading these properties. The increase in the apparent effective area and the improvement in the absorption losses are also given.

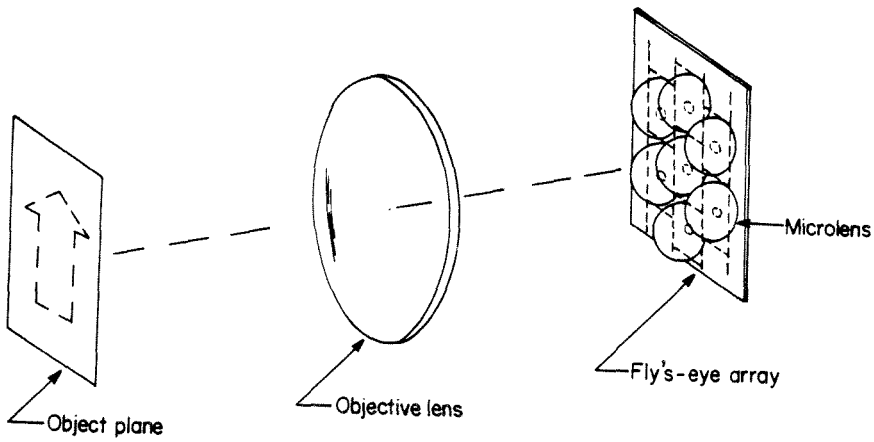

Figure 4.2 Fly's-eye imaging antenna array with small dielectric lenses.

4.1 Analysis of the Radiation Properties of Dielectric Lenses

Previously Zah *et al.* [7] used diffraction theory to find the focused fields in the substrate lens. They go on to calculate the coupling efficiency of a substrate-lens coupled imaging system. This approach is only valid when the radius of the lens is much larger than a free space wavelength. For spherical lenses, however, it is possible to solve Maxwell's equations directly, following Mie's theory of scattering by dielectric spheres [11]. However, previous work has concentrated on the scattered fields outside the sphere for an incident plane wave [12–14]. In this chapter the calculations are extended to find the fields inside the lens for a converging spherical wave (fig. 4.3). An extensive review of spherical dielectric antennas is given by Chatterjee [15]. The radiation from apertures in the presence of dielectric spheres has also been studied by previous investigators [16–18].

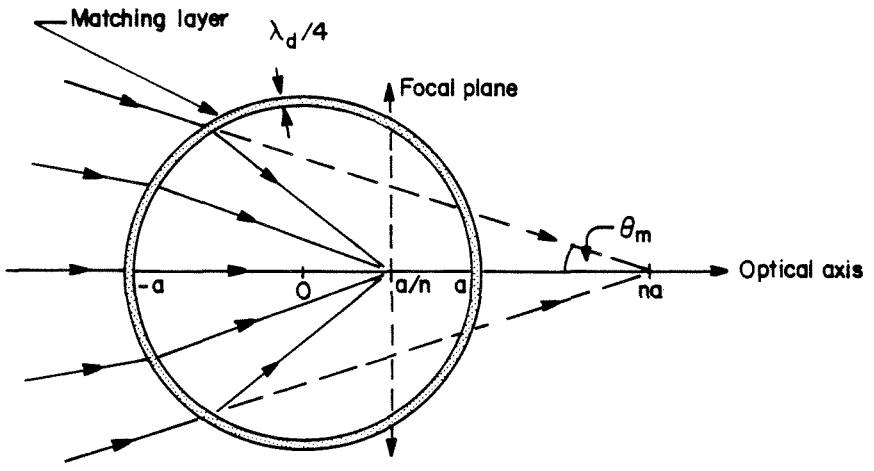

Figure 4.3 Spherical lens with matching layer. The lens has an aplanatic focal point which eliminates spherical aberration.

In this analysis the spherical lens is assumed to have a quarter-wave matching layer [19–20] as shown in Fig. 4.3. Although a quarter-wave matching layer does not give a perfect match for a spherical surface, it reduces the reflections at the

spherical interface considerably. Zah *et al.* [20] demonstrated a polystyrene cap on a silicon lens that almost eliminated the reflection losses - an improvement of about 1.5 dB. They also showed that the match was not very sensitive to the thickness of the cap.

Theory

Mie uses radial vector potentials to represent the fields inside and outside the sphere. The radial components of the vector potentials, which satisfy the scalar Helmholtz equation, are expanded in terms of spherical modes, consisting of spherical Bessel functions and associated Legendre functions [21–22]. The spherical mode expansion is an useful numerical technique for expressing arbitrary fields specified by analytical, experimental or numerical data. Ludwig [23] uses the spherical wave expansion for computing the near fields from far field patterns. The lens analysis is similar except that reciprocity is invoked to analyze the lens coupled antennas in reception rather than transmission. The losses may be accounted for by introducing a complex propagation constant.

The radial component of the electric vector potential outside the lens (region 1 in Fig. 4.4) may be written as

$$F_1(r,\theta,\phi) = \sum_{n=1}^{\infty} d_{n1} r\phi_{\mathrm{n}}(r,\theta,\phi) + \sum_{n=1}^{\infty} Z_n r(\psi_{\mathrm{n}}(r,\theta,\phi) + \phi_{\mathrm{n}}(r,\theta,\phi)) \qquad (4.1)$$

In the matching layer (region 2) this component is

$$F_2(r,\theta,\phi) = \sum_{n=1}^{\infty} c_{n2} r\psi_{\mathrm{n}}(r,\theta,\phi) + d_{n2} r\phi_{\mathrm{n}}(r,\theta,\phi) \qquad (4.2)$$

and outside the lens (region 3) it is

$$F_3(r,\theta,\phi) = \sum_{n=1}^{\infty} c_{n3} r(\psi_{\mathrm{n}}(r,\theta,\phi) + \phi_{\mathrm{n}}(r,\theta,\phi)) \qquad (4.3)$$

where

$$Z_n = j^{n-1} \frac{(2n+1)}{n(n+1)}$$

and ϕ_n and ψ_n are the nth spherical modes of the outward traveling wave and the inward traveling wave respectively. The c_{ni}'s and d_{ni}'s are constant coefficients. Note the potential in region 1 is written as a sum of a scattered wave and an incident plane wave. Z_n's are the coefficients of the incident wave. The magnetic vector potentials, $A_i(r, \theta, \phi)$ are also represented in a similar way.

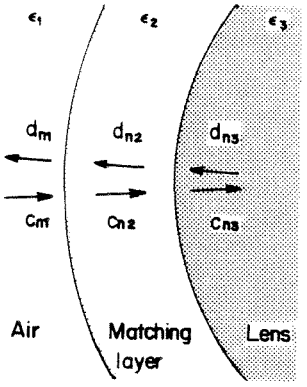

Figure 4.4 Outward and inward traveling waves in the three regions of a spherical lens.

The fields in each region are completely defined by these two potentials. c_{ni} and d_{ni} are found by applying the boundary conditions that the transverse electric field and the transverse magnetic fields are continuous at the interface. This results in four equations for each mode, two for the coefficients of the electric potential and two for the coefficients of the magnetic potential. The two equations for the coefficients for the electric potential at the interface between regions 1 and 2 may be written in matrix form as

$$\begin{pmatrix} h_n^{1\prime}(x) & h_n^{2\prime}(x) \\ k_1 h_n^1(x) & k_1 h_n^2(x) \end{pmatrix} \begin{pmatrix} Z_n \\ Z_n \end{pmatrix} + \begin{pmatrix} h_n^{1\prime}(x) & h_n^{2\prime}(x) \\ k_1 h_n^1(x) & k_1 h_n^2(x) \end{pmatrix} \begin{pmatrix} 0 \\ d_{n1} \end{pmatrix}$$

$$= \begin{pmatrix} h_n^{1\prime}(y) & h_n^{2\prime}(y) \\ k_2 h_n^1(y) & k_2 h_n^2(y) \end{pmatrix} \begin{pmatrix} c_{n2} \\ d_{n2} \end{pmatrix} \tag{4.4}$$

where h_n^1 and h_n^2 are the spherical Hankel functions representing inward traveling waves and outward traveling waves respectively. The primes represent derivatives of these functions. x and y are equal to $k_1 a$ and $k_2 a$ respectively. Equation (4) may rewritten as

$$\begin{pmatrix} h_n^{1\prime}(x) & h_n^{2\prime}(x) \\ k_1 h_n^1(x) & k_1 h_n^2(x) \end{pmatrix} \begin{pmatrix} c'_{ni} \\ d'_{n1} \end{pmatrix} = \begin{pmatrix} h_n^{1\prime}(y) & h_n^{2\prime}(y) \\ k_2 h_n^1(y) & k_2 h_n^2(y) \end{pmatrix} \begin{pmatrix} c_{n2} \\ d_{n2} \end{pmatrix} \tag{4.5}$$

where $c'_{n1} = Z_n$ and $d'_{n1} = d_{n1} + Z_n$. The spherical symmetry of the lens permits one to write such equations for each spherical mode.

By writing similar boundary conditions for the interface between regions 2 and 3, one may relate the outward traveling wave and the inward traveling wave in region 3 to the corresponding components in region 2 through a matrix equation similar to (4.5). The unknown coefficients c_{n3} and d_{n3}, for both the electric potential and the magnetic potential are found by solving the matrix equations. Having found the coefficients one may calculate the fields at any given point inside the sphere for an incident plane wave.

This analysis can extended to a converging beam from an objective lens by representing the converging beam in terms of its spatial frequency components. The spatial frequencies represent a spectrum of plane waves. Therefore the field component in the direction of incident polarization may be found as a superposition integral given by

$$e_y(r', \theta', \phi') = \frac{f E_i}{\lambda_0} \int_0^{2\pi} \int_{\cos\theta_m}^{1} e(x, \phi : \theta', \phi', r') \left(\sin^2\phi + x\cos^2\phi\right) \left(x^{-3/2}\right) dx d\phi \tag{4.6}$$

where x is equal to $\cos\theta$ and $e(x, \phi : \theta', \phi', r')$ is the field component in the direction of the incident polarization at some point (θ', ϕ', r') due to a plane in the direction given by (θ, ϕ). f is the focal length of the objective lens and θ_m is the angle shown in Fig. 4.3. This integral is very similar to the diffraction integral for the fields given by Zah *et al.* [7].

4.2 Results and Discussion

A computer program was written to calculate the electric fields and the magnetic fields inside the spherical lenses for different radii and dielectric constants. Formulas for the Bessel functions and the associated Legendre functions are given by Abramowitz and Stegun [22]. Since the fields are represented by an infinite sum of spherical modes, one has to truncate this series at some point. The series was truncated at the point at which doubling the number of modes produced a change of less than 1%. The required number of modes was found to be ten times the radius of the lens in free space wavelengths. Fig. 4.5 shows the calculated field at the geometrical focal point of a quartz lens ($\epsilon = 4$) of radius λ_0, for varying number of modes. This test was conducted for lenses of different radii and showed consistent results. The field is normalized by the field calculated from ten modes. On an IBM PC-AT the time taken to calculate the contribution due to a single mode was approximately one second.

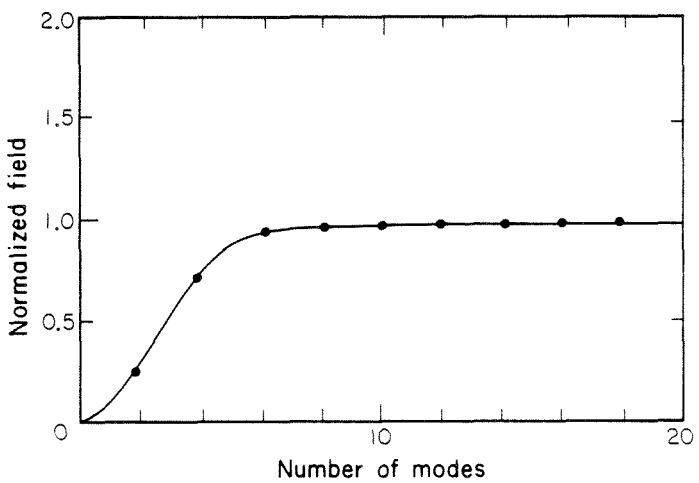

Figure 4.5 The normalized field calculated from different numbers of modes for $\epsilon = 4$ and $a = \lambda_0$.

Results are plotted in terms of a normalized intensity which was called the focusing gain. The focusing gain is defined as the ratio of the component of

the Poynting vector along the optical axis at the point of observation to the corresponding component at the geometrical focal point in the absence of the substrate lens. The focusing gain reflects the factor by which the effective area of the antenna will increase in the presence of the lens.

Figs. 4.6 and 4.7 show the maximum focusing gain along the optical axis plotted as a function of the lens radius for silicon and quartz respectively. It also shows the distance of this maximum from the center of the sphere. The geometrical *f-number*, $f_{\#}$ inside the lens was taken to be 0.6 for all the lenses. The first plot reflects the degradation in the focusing when the lens radius is made small. For silicon ($\epsilon = 12$) the gain falls off rapidly when the radius is smaller than one free space wavelength. For quartz ($\epsilon = 4$) the gain falls off when the radius is smaller than a half of the free space wavelength. These values are the minimum radii at which the lenses exhibit good focusing properties. Rutledge *et al.* showed that to get diffraction limited imaging using coherent field detection, the sampling distance had to be less than the product of the $f_{\#}$ and the wavelength of the imaging medium. In this work this results in sampling distances of $1.2\lambda_0$ for quartz and $2\lambda_0$ for silicon. As the minimum diameters for lenses of these two materials are comparable with these values, one may use these lenses in the fly's-eye configuration and expect to achieve close to diffraction limited imaging.

The ripples in the curve are due to resonances of the spherical modes and have been studied by Kerker [12]. The effect is more noticeable for large dielectric constants. When the radius of the lens is increased the resonant intensities become smaller. In the limit, the maximum focusing gain will tend towards the geometric gain. The geometric gain is the factor by which the maximum intensity is increased when the power is coupled through a large substrate lens. It is equal

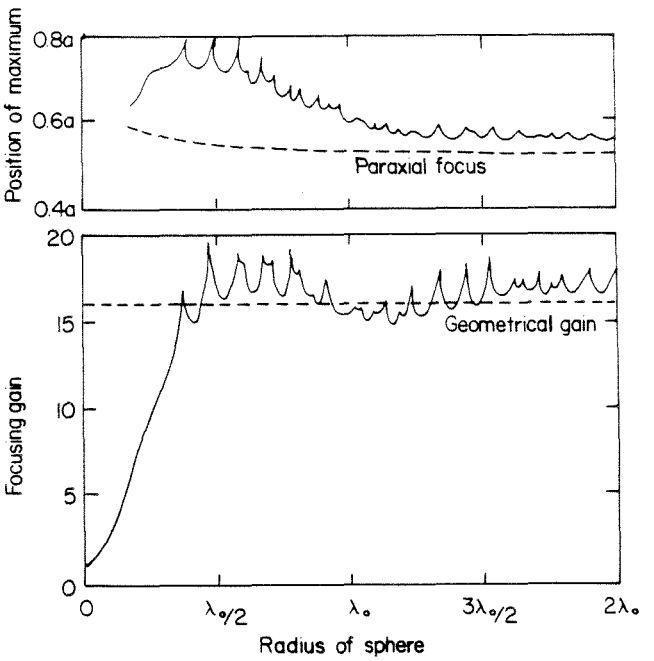

Figure 4.6 The maximum focusing gain plotted against the radius of the lens for silicon ($\epsilon = 12$). Also shown is the position of the maximum.

to the square of the dielectric constant.

In the secondary plot one observes that for lenses of small radii the power is focused further away from the center of the sphere. Clearly the antennas will have to be built at this position to obtain good coupling. The resonances of the spherical modes show up as spikes in these curves too. For large radii the curves tend towards the geometrical focal point.

Fig 4.8 shows the focusing gain plotted along the optical axis for lenses of different radii for silicon and quartz. The humps on the optical axis reflect the focusing power of the lenses. One observes that the focusing properties of larger lenses tend towards the results derived from diffraction theory. This is to be expected from the correspondence between the electromagnetic solution and the

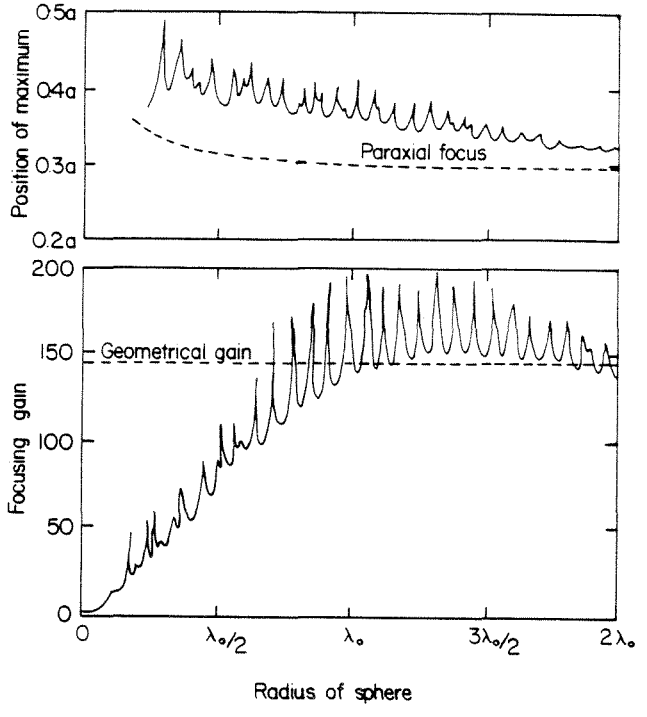

Figure 4.7 The maximum focusing gain plotted against the radius of the lens for quartz ($\epsilon = 4$). Also shown is the position of the maximum.

optics solution. Another interesting feature in these curves is the absence of standing waves, clearly indicating that most of the power is in the forward going wave and the back surface has little effect. One may conclude from this observation that these lenses and the hyperhemispheric lenses have similar focusing properties. In the absence of the matching layer, the standing waves were found to be more pronounced.

Fig. 4.9 shows the focusing gain in the focal plane, which is the plane on which the axial power is a maximum. One may observe that these patterns resemble Airy patterns which may be obtained from Fraunhofer diffraction theory [24]. Fraunhofer diffraction theory applies only to systems with large $f_{\#}$'s and large axial distances. In most of these calculations the $f_{\#}$ inside the substrate lens

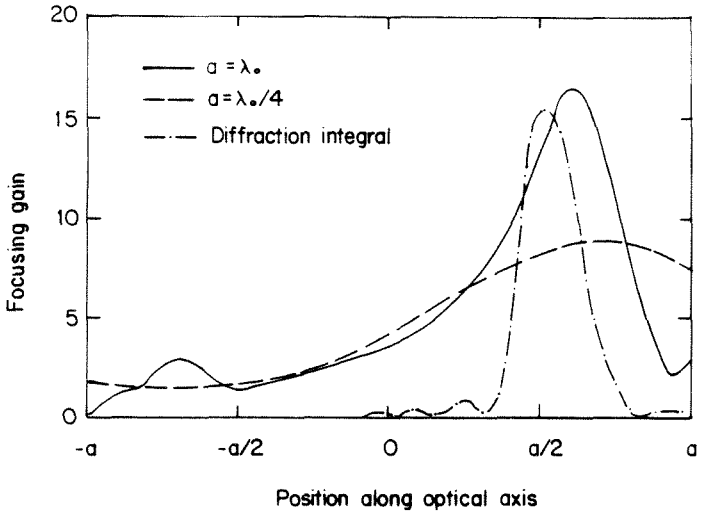

(a)

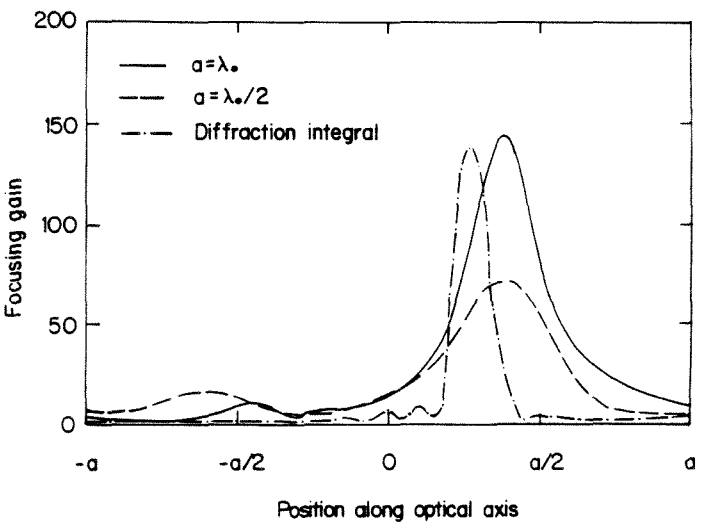

(b)

Figure 4.8 The focusing gain along the optical axis of a small lens for (a) $\epsilon = 4$ and (b) $\epsilon = 12$.

is less than 1. Therefore it is interesting to note that the deviation is minimal especially when the lens radius is larger than the minimum radius. The shape of the field pattern in the focal plane will determine what type of antenna one must use as a receptor in the imaging array.

Fig. 4.10 shows the absorption losses at 94 GHz plotted for three different lens materials as a function of the lens radius. The absorption coefficients are

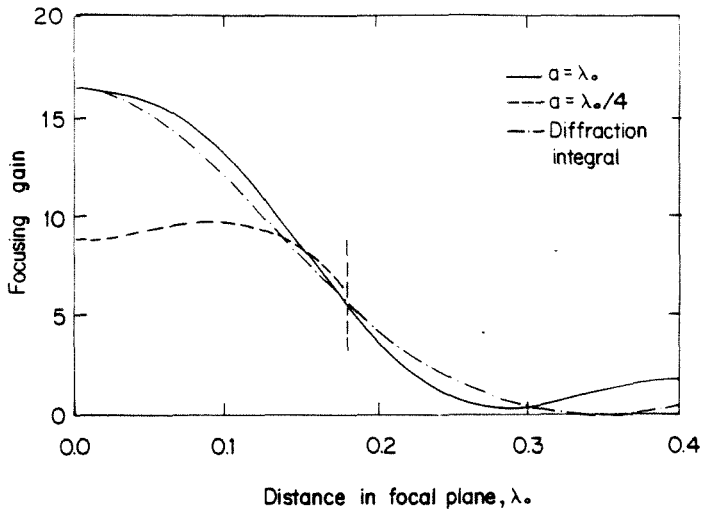

(a)

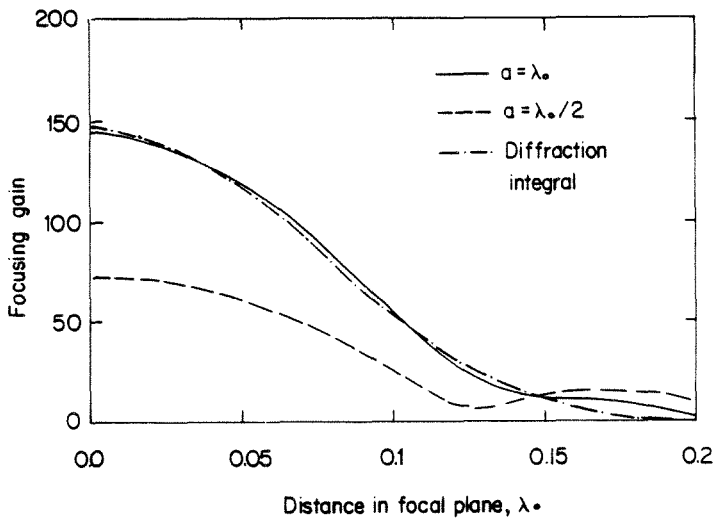

(b)

Figure 4.9 The focusing gain in the focal plane of a small lens for (a) $\epsilon = 4$ and (b) $\epsilon = 12$.

taken from Afsar and Button [9]. The losses in the matching layer are neglected in all the calculations. The losses were extremely small for lenses of small radii. For silicon lens of the minimum radius, λ_0, the losses are 0.2 dB. For a fused quartz lens of radius $\lambda_0/2$ the losses were even smaller, about 0.02 dB. For comparison, Zah estimated the losses of his lens of radius 1.2cm to be about 1 dB at 94 GHz. The absorption loss is close to that of a plane wave propagating through a slab

of the same material, with a thickness of $(n+1)a/n$. This is the distance from the front of the lens to the geometric focus.

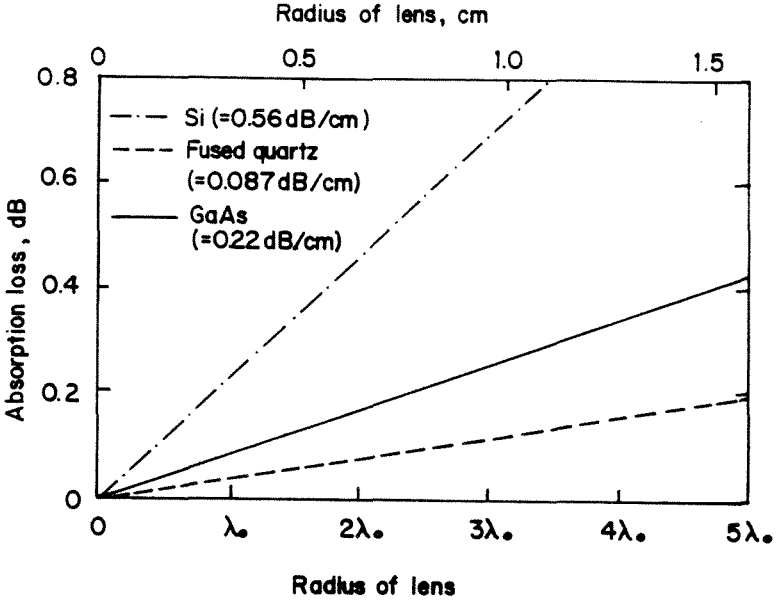

Figure 4.10 Absorption losses of small lenses at 94 GHz, for fused quartz, silicon and GaAs. Absorption coefficients from Afsar and Button [9].

Fig. 4.11 shows the coupling efficiencies of a lens coupled dipole with a silicon lens of radius $1\lambda_0$ for different *f-numbers*. The coupling efficiency was calculated by using a method similar to Zah *et al.* [7]. For comparison the coupling efficiencies of a large silicon lens coupled dipole (from Zah *et al.* [7]) and the coupling efficiencies of a dipole in free space are also given. The coupling efficiency is essentially the efficiency of coupling between the incident radiation on the primary lens and the antenna [7,23]. The dipole in free space loses 50% efficiency off the top because it radiates in both directions. The lens coupled dipoles do not have this degradation in their performance because the radiation into air is negligible. The coupling efficiency of the small lens coupled dipole is almost as good as the large lens coupled dipole. At large $f_{\#}$'s it is in fact slightly better than the large lens coupled dipole. This could be due to the resonances of the small lens having

a constructive influence on the field at the focal point. The efficiency of the small lens coupled dipole is greater than 40% for $f_{\#}$'s less than 0.7.

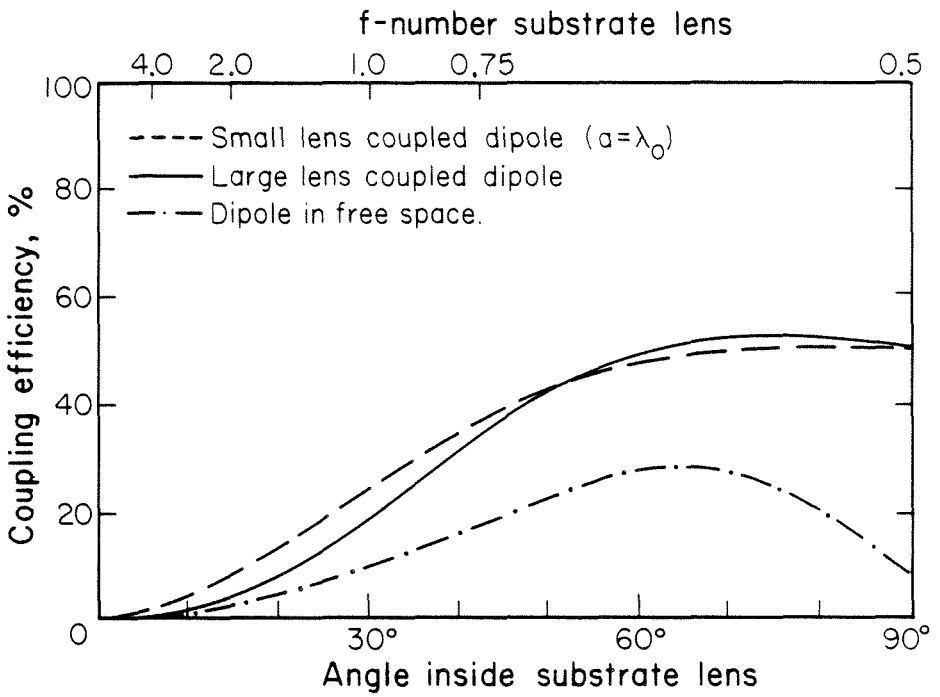

Figure 4.11 The coupling efficiencies of a silicon lens coupled dipole with $a = \lambda_0$ for different $f_{\#}$'s. Also shown are the coupling efficiencies of a large silicon lens coupled dipole [7] and a dipole in free space.

Fig. 4.12 shows the smallest useful radius of the lens plotted as a function of the refractive index of the lens. The curve seems to have a linear dependance on the refractive index. The sampling distance for coherent diffraction limited imaging is given by [1]

$$T_E = \frac{\lambda_0}{n_1} f_{\#} \tag{4.7}$$

where λ_0 is the free space wavelength and n_1 is the refractive index of the medium the image is formed in. Now in the fly's-eye configuration the imaging is done in

free space. Therefore the sampling distance is given by

$$T_E = \lambda_0 f_{\#} \tag{4.8}$$

From Fig. 4.12 one may conclude that for an $f_{\#}$ of 2 in air (corresponds to an $f_{\#}$ of 0.6 in silicon) diffraction limited imaging will be possible with small lenses with refractive indices up to about 5.

In systems where the diameter of the substrate lens is much smaller than the spot size of the primary lens, the coupling of power was found to be small. This is because when the lens is smaller than the spot size, not all the power in the primary beam is incident on the lens. In a fly's-eye array this will also lead to a degradation in resolution due to the spot size being larger than the resolution cell. Therefore it is important that the lens radius is not too much smaller than the spot size at the focal plane of the primary lens. The field distribution near the focal plane of the primary lens is given by Born and Wolf [25].

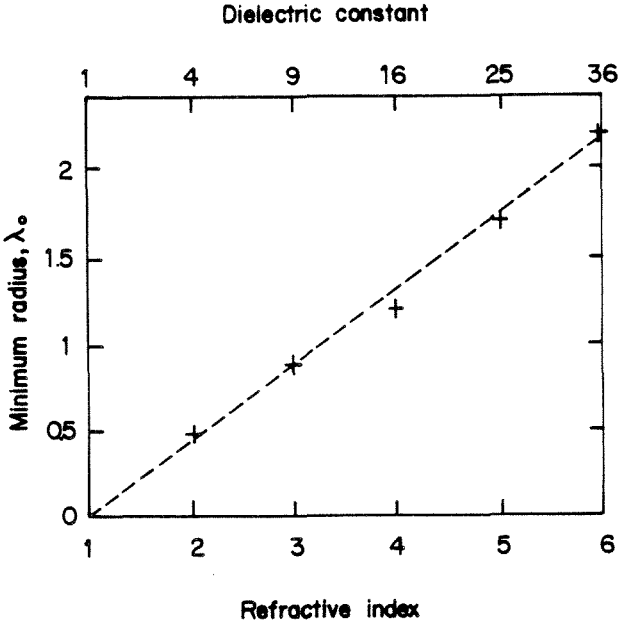

Figure 4.12 The minimum useful radius plotted against the refractive index of the lens.

4.3 Conclusion

The calculations indicate that the small lenses may be used as good focusing elements down to radii comparable with the free space wavelength. For fused quartz one may go down to about half a free space wavelength and still maintain good focusing properties. Similarly for silicon this radius is about one free space wavelength. For large lenses the focusing gain approaches the geometric gain which is equal to the square of the dielectric constant. The absorption losses of the small lenses at 94 GHz are considerably smaller than those of larger lenses. For a silicon lens of radius $1\lambda_0$ these losses were 0.2 dB and for quartz lens of radius $\lambda_0/2$ the losses were about 0.02 dB. Finally the coupling efficiency of a silicon lens coupled dipole with a lens radius of λ_0, does not show any degradation in comparison to a large silicon lens coupled dipole.

References.

[1] D. B. Rutledge, D. P. Neikirk, D. P. Kasilingam, "Integrated Circuit Antennas," *Infrared and Millimeter Waves*, **10**, pp. 1–90, K. J. Button, ed., Academic Press, Inc., New York, 1983.

[2] P. E. Young *et al.*, "Multichannel Far-Infrared Phase Imaging for Fusion Plasmas," *Rev. Sci. Instrumen.*, **56**, pp. 81–89, 1985.

[3] C. E. Zah *et al.*, "Millimeter-Wave Monolithic Schottky Diode Imaging Arrays," *Intl. J. of Infrared and Millimeter Waves*, **6**, pp. 981–997, 1985.

[4] M. J. Wengler *et al.*, "A Low Noise Receiver for Millimeter and Submillimeter Wavelengths," *Intl. J. of Infrared and Millimeter Waves*, **6**, pp. 689–696, 1985.

[5] B. J. Clifton *et al.*, "High Performance Quasi-Optical GaAs Monolithic Mixer at 110 GHz," *IEEE Trans. Electron Devices*, **ED-28**, pp. 155–157, 1981.

[6] N. G. Alexopoulos, P. B. Katehi, D. B. Rutledge, "Substrate Optimization for Integrated Circuit Antennas," *IEEE Trans. Microwave Theory Tech.*, **MTT-31**, pp. 550–557, 1983.

[7] C. E. Zah, R. C. Compton, D. B. Rutledge, "Efficiencies of Elementary Integrated Circuit Antennas," *Electromagnetics*, **3**, pp. 239–254, 1983.

[8] D. P. Neikirk, "Integrated Detector Arrays for High Resolution Far-Infrared Imaging," *PhD Thesis Dissertation*, California Institute of Technology, Pasadena, 1983.

[9] M. N. Afsar, "Dielectric Measurements of Millimeter-Wave Materials," *IEEE Trans. Microwave Theory Tech.*, **MTT-32**, pp. 1598–1609, 1984.

[10] R. C. Compton, G. M. Rebeiz, D. B. Rutledge, "Developments in Two-Dimensional Arrays," *10th Intl. Conf. on Infrared and Millimeter Waves*, pp. 277–278, 1985.

[11] G. Mie, *Ann. of Physics*, **25**, pp. 377–445, 1908.

[12] M. Kerker, *The Scattering of Light and Other Electromagnetic Radiation*, Academic Press, New York, pp. 27–96, 1969.

[13] H. C. van de Hulst, *Light Scattering by Small Particles*, John Wiley, New York, pp. 63–81, 1957.

[14] M. Born, E. Wolf, *Principles of Optics*, Pergamon Press, Oxford, pp. 635–647, 1980.

[15] R. Chatterjee, *Dielectric and Dielectric Loaded Antennas*, Research Studies Press, Letchworth, England, pp. 135–187, 1985.

[16] M. S. Narasimhan, S. Ravishankar, "Radiation from Aperture Antennas Radiating in the Presence of a Dielectric Sphere," *IEEE Trans. Antennas Propagat.*, **AP-30**, pp. 127–1240, 1982.

[17] W. F. Crosswell *et al.*, "Radiation from a Homogeneous Sphere Mounted on a Waveguide Aperture," *IEEE Trans. Antennas Propagat.*, **AP-23**, pp. 647–656, 1975.

[18] A. G. Martin, A. J. A. Oxtoby, "Waveguide Fed Spherical Dielectric Antennas," *IEEE Trans. Antennas Propagat.*, **AP-22**, pp. 338–339, 1974.

[19] K. R. Armstrong, F. J. Low, "Far-Infrared Filters Utilizing Small Particle Scattering and Antireflection Coatings," *Appl. Optics*, **13**, pp. 425–430, 1974.

[20] C. E. Zah, D. B. Rutledge, "A Polystyrene Cap for Matching a Silicon Lens at Millimeter Wavelengths," *Intl. J. of Infrared and Millimeter Waves*, **6**, 1985.

[21] R. F. Harrington, *Time Harmonic Electromagnetic Waves*, McGraw-Hill, New York, 1961.

[22] M. Abramowitz, I. Stegun, *A Handbook of Mathematical Functions*, Dover

Publications, New York, 1964.

[23] A. C. Ludwig, "Near Field and Far Field Transformation Using Spherical Wave Expansions," *IEEE Trans. Antennas Propagat.*, **AP-19**, pp. 210–214, 1971.

[24] J. W. Goodman, *Introduction to Fourier Optics*, McGraw-Hill, New York, pp. 48–54, 1968.

[25] M. Born, E. Wolf, *Principles of Optics*, Pergamon Press, Oxford, pp. 435–449, 1980.

CHAPTER 5.

Two-Dimensional Horn Arrays for Diffraction Limited Imaging.

Several non-scanned imaging systems using fast, sensitive detection by focal plane devices at millimeter-wave frequencies have been developed in recent years [1–3]. Most of these systems use quasi-optical imaging techniques [4] utilizing either a parabolic dish or a lens [5–7] as the primary antenna. Yngvesson [8] discusses the advantages and the disadvantages of reflector and lens systems. In focal plane systems it is crucial that one has good feed antennas that couple efficiently to the primary antenna. A considerable amount of work has been done in studying planar antennas and antenna arrays as possible feed antennas [9–11].

In high resolution imaging arrays, not only must the antennas couple efficiently to the primary antenna but they also have to be in close proximity to each other to satisfy the sampling requirements. The first condition requires that the antennas have effective areas comparable to their physical size. Schwarz [12] and Zah *et al.* [13] have studied the coupling efficiencies of feed antennas. It can be shown that to maximize the coupling the antenna beam pattern of the feed antenna should match the pattern of the incident radiation [12]. The second condition requires the antennas be small, thereby reducing their effective area. In addition, for two-dimensional arrays there is also a problem of space for low-frequency lines [11]. Therefore the design objective is to be able to build a two-dimensional imaging array consisting of small antennas placed in close proximity to each other, while also maintaining good coupling efficiencies. As mentioned in the previous chapter, one solution would be a multiple lens-coupled array. In this chapter I look at another possible design which uses a two-dimensional array of small horns etched into crystalline silicon.

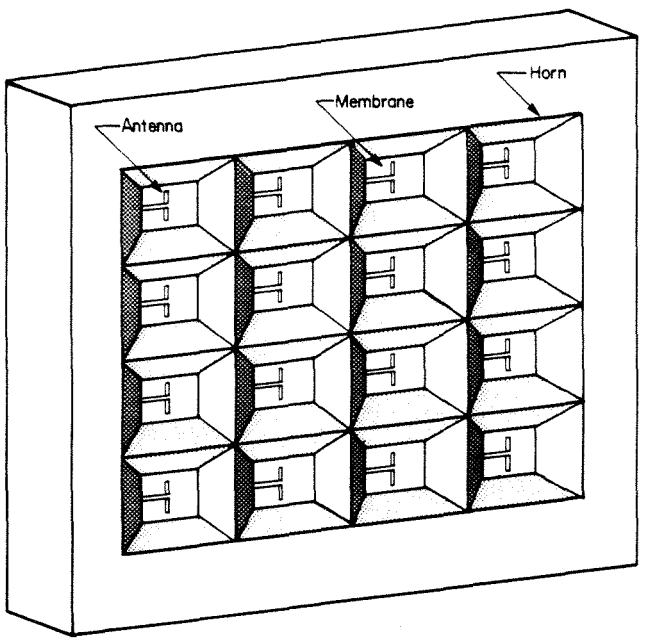

Figure 5.1 Two-dimensional imaging array consisting of pyramidal horns etched into highly doped crystalline silicon. The antennas are built on a silicon nitride membrane.

Arrays of planar log-periodic antennas on thin membranes have been built and tested successfully in the past year [14]. This came about because of a need to build far-infrared imaging arrays which did not use lossy substrate lenses. The highly successful work on antennas on thin membranes gave rise to the idea of two-dimensional horn arrays. Fig. 5.1 shows such an array. The plan is to deposit a thin layer, about $10\mu m$ of silicon nitride on a crystalline silicon substrate and then etch through the silicon until only a thin membrane of silicon nitride is left. Another piece of silicon is etched to form the back short. The etching of silicon occurs along the $\langle 111 \rangle$ plane resulting in a pyramidal structure with a horn half-angle of 35.3° as shown in Fig. 5.2(a). The highly doped silicon walls will appear 'metallic' at the design frequencies. The membranes will be used to build planar feed antennas and other supporting circuitry. An additional advantage of this

method is that by using many such etched silicon wafers on top of each other with a slight mismatch at the boundary, one may introduce corrugations inside the horn as shown in Fig. 5.2(b).

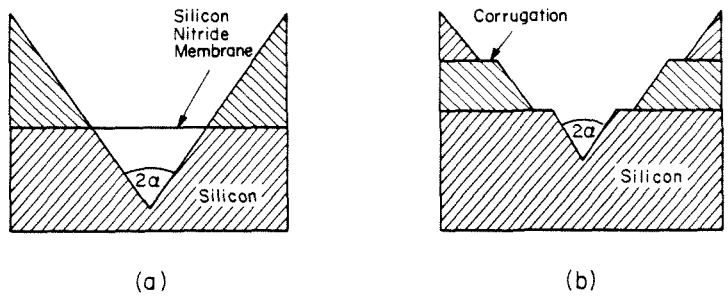

Figure 5.2 (a) Cross-section of horn etched into silicon. (b) Cross-section of corrugated horn with many different silicon wafers (the corrugations are exaggerated). Horn half-angle, $\alpha = 35.3°$.

In this chapter, the pyramidal horn array is analyzed to study the coupling efficiencies of these horns and to design a possible diffraction limited imaging system. As the horn dimensions are comparable with the free space wavelength, the array has to be analyzed rigorously using a complete electromagnetic solution. Love [15], in an excellent collection of papers, reflects the development of horn antennas over the years. In the past, investigators have used diffraction theory to predict the radiation properties of pyramidal horns and sectoral horns [16–18]. Unfortunately these methods of analysis are not valid for horns with large horn angles and short axial lengths. In addition, in a horn array, the horn elements tend to couple with each other, especially when the array spacing is small.

Rectangular horn arrays and rectangular waveguide arrays have been analyzed by Amitay and his co-workers [19–21]. Most of their work has been documented in their authoritative text on phased arrays [22]. Even though they

analyze their arrays incorporating the ideas of electromagnetic grating theory [23], they make approximations which make their analysis not valid for horns with large flare angles. The small flare angle approximation assumes that the coupling between the different modes in a horn element is negligible. In our analysis using the stepped waveguide method this coupling was found to be significant.

The chapter starts with a review of the sampling requirements for diffraction limited imaging. In the next section I analyze one-dimensional groove arrays. In this section the groove array is analyzed as a possible configuration for diffraction limited imaging arrays. This analysis also helps to estimate the performance of two-dimensional arrays. The final section looks at two-dimensional pyramidal horn arrays. The radiation pattern and the gain of a single horn element in the array and its coupling efficiency to the primary lens antenna are calculated so as to design a two-dimensional imaging array.

5.1 Sampling for Diffraction Limited Imaging.

All imaging systems have finite resolving power. This results in the system acting as a low-pass spatial filter, that is the spatial frequency components of the image will contain frequency components less than some system cutoff frequency. In diffraction limited imaging, one designs an imaging array that samples the image at such a rate that the resolution of the reconstructed image is limited only by the resolving power of the optical system. The reconstruction algorithm given by the Whittaker-Shannon sampling theory [24] is

$$g(x) = \sum_{n=-\infty}^{\infty} g\left(\frac{n}{2f_0}\right) \operatorname{sinc}\left[2f_0\left(x - \frac{n}{2f_0}\right)\right], \tag{5.1}$$

where $g(x)$ is either the complex field E or the intensity I. The function $g\left(\frac{n}{2f_0}\right)$ is the sampled image points separated by $1/2f_0$, f_0 the spatial cutoff frequency

and $\mathrm{sinc}(x) = (\sin \pi x)/\pi x$.

In this chapter the cutoff frequency f_0 implies that the optical system passes all spatial frequency components of the field $\mathbf{E}(x)$ up to f_0. Now because the intensity, $\mathbf{I}(x)$ is given by the square of the field it will contain frequency components up to $2f_0$. Therefore the Nyquist criterion would require that for field sampling the maximum separation of sampling points be $1/2f_0$ and for intensity sampling, like in video detection, the sampling distance should be less than $1/4f_0$.

Born and Wolf [25] show that the cutoff frequency in the image plane is

$$f_0 = \frac{n_1 \sin \theta_1}{\lambda_0}, \tag{5.2}$$

where n_1 is the index of refraction of the medium in which the image is formed, θ_1 is the half angle subtended by the exit pupil (Fig. 5.3) and λ_0 the free space wavelength. It can be shown [24] that for objects far from the entrance pupil the image point approaches the focal point, and the *f-number* ($f_\#$) of the optics is then related to θ_1 by

$$f_\# = \frac{1}{2 \sin \theta_1} \tag{5.3}$$

From equations 5.2 and 5.3 one gets the sampling distances as

$$T_E = \frac{\lambda_0}{n_1} f_\#, \tag{5.4}$$

for field detection and

$$T_I = \frac{\lambda_0}{2n_1} f_\#, \tag{5.5}$$

for intensity detection.

In calculating the $f_\#$ of the optical system, it is important all the optical elements be taken into account. For instance, the $f_\#$ of a substrate coupled imaging system is related to that of a imaging system in free space by

$$f_\#^s = \frac{f_\#^0}{n_1}, \tag{5.6}$$

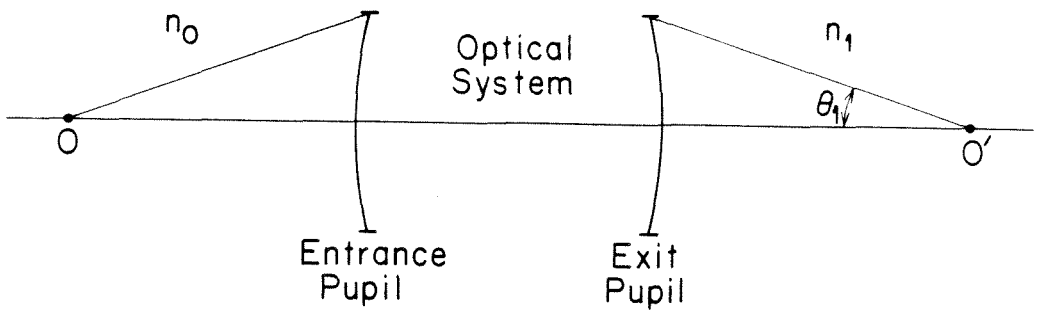

Figure 5.3 Optical system showing the extreme ray path into the entrance pupil and out of the exit pupil.

where $f_{\#}^{s}$ and $f_{\#}^{0}$ are the $f_{\#}$'s of the substrate coupled imaging array and the free space imaging array respectively and n_1 the index of refraction of the substrate lens. Rutledge *et al.* [26] describe methods of imaging coherent and incoherent images.

The sampling criterion as shown above restricts the distance between the image points. This means that the antennas have to be in close proximity to attain diffraction limited imaging. The sampling distance T_E (and T_I) is proportional to the $f_{\#}$. Therefore for imaging systems with small $f_{\#}$ the antenna spacing becomes small and may not be physically realizable. Most optical systems are a compromise between small $f_{\#}$ systems necessary for high image resolution and large $f_{\#}$ systems required for minimizing aberrations. Such a system would require that the antenna spacing be of the order of a free space wavelength. In the next section arrays with spacing comparable with the free space wavelength are analyzed.

5.2 One-Dimensional Groove Arrays.

Several one-dimensional imaging arrays have been made both at millimeter

and near millimeter frequencies [1–2]. In this section a one-dimensional imaging array consisting of small antennas placed in *V*-shaped grooves (Fig. 5.4) is analyzed. The *V*-shaped groove acts as a focusing element similar to a reflector antenna. *V*-shaped grooves have been used before as corner reflectors [7,27]. Fabrication methods developed in the millimeter-wave integrated circuits laboratory allows one to make these arrays of *V*-shaped grooves by etching crystalline silicon [28]. Rebeiz *et al.* [14] developed a fabrication process to build planar antennas on thin membranes. This process allows one to build the feed antennas on thin membranes inside the groove.

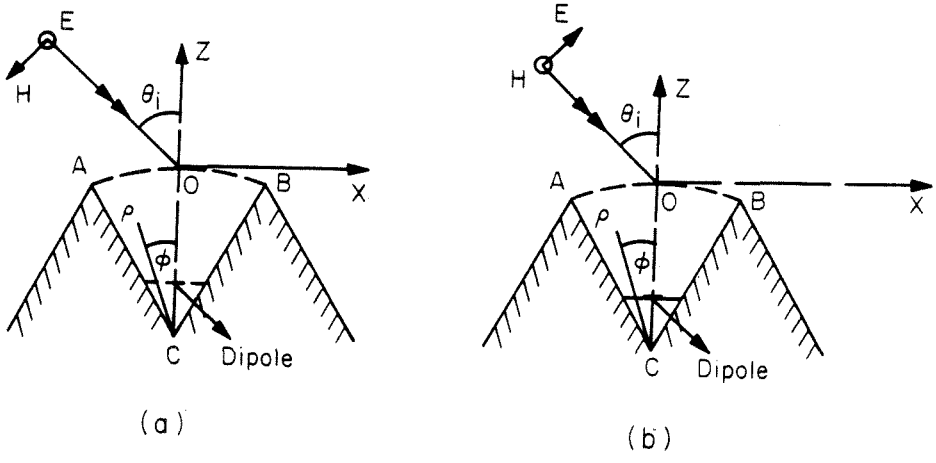

Figure 5.4 One-dimensional horn array with (a) dipole aligned parallel to groove (b) dipole aligned perpendicular to groove.

In this section the one-dimensional groove antenna array is analyzed using a rigorous and an approximate electromagnetic solution. The array of V-shaped grooves, because of its cylindrical configuration and its periodicity, is amenable to a complete electromagnetic solution. The fields inside the groove are represented by cylindrical modes [29] and the fields outside by Floquet modes [23,30]. The radiation pattern is found by reciprocity by calculating the response to plane waves at different angles of incidence. In all the calculations the antennas are

assumed to be small and that they do not affect the fields inside the groove. The arrays are also assumed to be infinite so that the fields are given completely by Floquet modes. The approximate method is the stepped waveguide method where the groove is sectioned into short lengths of parallel plate waveguides. In this method the fields inside the groove are given by a combination of the waveguide modes. In the limit, this approximation should give the same results as the cylindrical wave function method. The results of the one-dimensional V-groove array also allows one to estimate the performance of two-dimensional pyramidal horn arrays.

Analysis Using Cylindrical Wave Functions.

The fields inside the groove may be represented by electric and magnetic vector potentials along the direction of the groove (Fig. 5.4). The choice of vector potential will depend on the polarization of the feed antennas. In all the calculations it is assumed that the feed antenna is a linearly polarized antenna aligned parallel to the grooves or perpendicular to the grooves as shown in Fig. 5.4 (a) and 5.4 (b) respectively. The former case will require electric potentials to represent the fields inside the groove and the latter magnetic potentials if the incident plane wave is in the classical diffraction plane [31] which is the plane normal to the groove axis. From Harrington [29] the potential functions inside the groove are

$$F_1 = \sum_{m=0}^{\infty} a_m \psi_m(\rho, \phi), \tag{5.7}$$

where

$$\psi_m(\rho, \phi) = \frac{1}{\sqrt{\alpha}} J_v(k_0\rho) \begin{matrix}\sin \\ \cos\end{matrix}(v(\phi - \alpha)), \tag{5.8}$$

$$v = \frac{m\pi}{2\alpha},$$

$J_v(k_0\rho)$ is the Bessel function of order v, k_0 the free space propagation constant and α the half-angle of the groove (Fig. 5.4). The sine dependance occurs for

TE modes and the cosine dependence for the TM modes. There is no variation in the y-direction. In this design the angle α is constrained to be equal to 35.3° because the etching is conducted along the $\langle 111 \rangle$ plane.

The fields in air may be represented by potentials of Floquet modes which are given by

$$F_2 = \sum_{n=-\infty}^{\infty} b_n \, \phi_{n+}(x,z) \; + \; c_0 \, \phi_{0-}(x,z), \tag{5.9}$$

where

$$\phi_{n+}(x,z) = \frac{1}{\sqrt{c_0}} exp - j(\alpha_n x + \gamma_n z), \tag{5.10}$$

$$\phi_{0-}(x,z) = \frac{1}{\sqrt{c_0}} exp - j(\alpha_0 x - \gamma_0 z), \tag{5.11}$$

$$\alpha_n = \alpha_0 + \frac{2n\pi}{c_0},$$

$$\gamma_n = \sqrt{k_0^2 - \alpha_n^2},$$

$$\alpha_0 = k_0 \sin\theta_i.$$

$\phi_{n+}(x,z)$ represents the reflected modes and $\phi_{0-}(x,z)$ the incident mode. c_0 is the aperture size.

Having found the fields in terms of these potential functions, one solves for the boundary conditions. The boundary in this case is the arc AOB as shown in Fig. 5.4. This boundary was chosen for computational expediency, because this would require only one value of the Bessel function and its derivative. The computation of the Bessel functions take considerably more time than the computation of Floquet modes. Galerkin's method of moments [32–33] is utilized to get a set of linear equations with the modal coefficients as the unknowns. One has to truncate the infinite series at some point to arrive at a numerical solution. As expected, this number was found to be dependent on the size of the grooves in terms of wavelengths. The number of modes N_0, beyond which the error in the field strength was less than 1% was found to be ten times the radial distance.

The matrix form of the linear equations for the electric fields at the boundary is

$$\mathbf{a} = \mathbf{U}\,(\mathbf{b} + \mathbf{c}) \tag{5.12}.$$

where a, b and c are vectors representing the coefficients of the potentials of the fields inside the groove, the reflected fields in air, and the incident fields in air respectively. For the TE modes, the elements of the matrix U are given by

$$U_{mn} = \frac{1}{\sqrt{\alpha c_0} J_v(k_0\rho)} \int_{-\alpha}^{\alpha} \sin(v(\phi - \alpha))\, e^{j(\alpha_n x + \gamma_n z)}\, d\phi \tag{5.13}$$

Similarly the equations for the magnetic fields are given by

$$\mathbf{a} = \mathbf{U}'\,(\mathbf{b} - \mathbf{c}) \tag{5.14}$$

where the elements of the matrix U' are given by

$$U'_{mn} = \frac{1}{\sqrt{\alpha c_0} J'_v(k_0\rho)} \int_{-\alpha}^{\alpha} \sin\left(v(\phi - \alpha)\right) e^{j(\alpha_n x + \gamma_n z)} \left(\frac{\gamma_n}{k_0}\cos\phi + \frac{\alpha_n}{k_0}\sin\phi\right) d\phi \tag{5.15}$$

Similar equations may be written for the TM modes in the other configuration.

By manipulating the matrix equations (5.12) and (5.14) one may find either the coefficients of the reflected fields b, or the coefficients of the fields inside the groove a, as a linear combination of the incident fields. In all the calculations reciprocity is invoked to find radiation patterns and coupling efficiencies. If one finds the fields inside the groove for a given set of incident waves, then from reciprocity one may find the transmitted fields and power. Using reciprocity the transmitted fields at a distance R in a given direction for an infinitesimal dipole of length h and current I_0 is given by

$$E_t(\theta, \phi) = \frac{\eta_0}{2R}\, e(\theta, \phi) \left(\frac{h}{\lambda_0}\right) I_0 \tag{5.16}$$

where η_0 is the free space wave impedance and $e(\theta, \phi)$ the field strength at the dipole for a unit plane wave incidence.

The following tests were conducted for convergence and accuracy.

(1) Conservation of power – the sum of power in all the propagating reflected modes has to be equal to the sum of the power in all the incident modes.

(2) Reciprocity theorem – the coupling efficiencies between any two propagating modes should be the same.

(3) The fields at the boundary calculated from the cylindrical potential functions should be equal to the fields at the boundary calculated from the Floquet mode representation.

(4) The field calculated using N_0 modes should be less than 1% off the fields calculated using 10 N_0 modes. This is a test for convergence.

Analysis Using Stepped Waveguide Approximation.

In this section an approximate method for analyzing the V-shaped grooves is introduced. Fig. 5.5 shows a V-shaped groove sectioned into parallel plate waveguides of varying heights. When the length of these sections is small this structure will look like a V-shaped groove. This type of approximation has been used before for analyzing gratings [34] and more recently rectangular horns [35]. I analyze the parallel plate structure in this section for two reasons. This approximation involves simple potential functions consisting of sines and cosines which help to reduce the computation time considerably. The other reason is to be able to check the validity of this approximation, so that a similar rectangular waveguide type of approximation may be applied to the pyramidal horn in the next section. Unlike the V-shaped grooves the pyramidal horns do not have any known analytical potential functions. Therefore by analyzing the accuracy of the parallel plate approximation, one is able to estimate the accuracy of the rectangular waveguide approximation. In addition the stepped waveguide method provides greater insight into the physics of this problem.

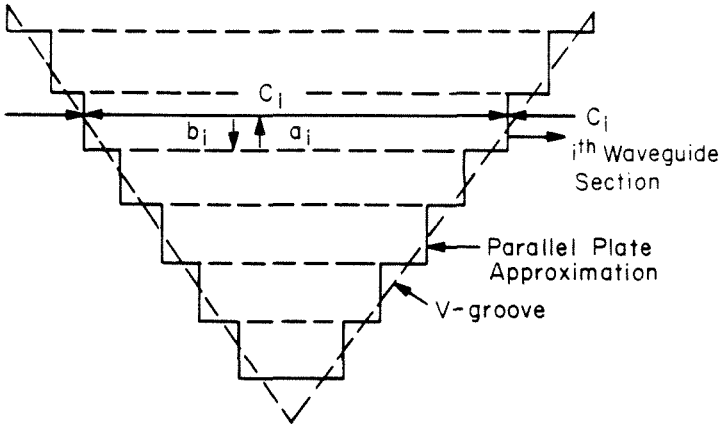

Figure 5.5 Stepped waveguide method – *V*-groove sectioned into parallel plate waveguides. $\mathbf{a_i}$ and $\mathbf{b_i}$ are the waves traveling in the positive z-direction and the negative z-direction, in the ith waveguide section.

The fields in air are represented by the same Floquet modes as in the previous section (eq. 5.9). The fields in the ith parallel plate waveguide section are given by the potential function [36]

$$F_1^i = \sum_{m=0(1)}^{\infty} (a_m \psi_{m+}^i(x,z) + b_m \psi_{m-}^i(x,z)), \tag{5.17}$$

where

$$\psi_{m\pm}^i(x,z) = \sqrt{\frac{(2-\delta_{0m})}{c_i}} \begin{matrix}\sin(k_m x)\\ \cos(k_m x)\end{matrix} exp(\mp j\gamma_m z), \tag{5.18}$$

$$k_m = \frac{m\pi}{c_i},$$

$$\gamma_m = \sqrt{k_0^2 - k_m^2},$$

and c_i is the height of the waveguide section. The index in brackets applies to the TE modes. The sine dependence applies to odd TM modes and even TE modes while the cosine dependence applies to even TM modes and odd TE modes. The TM_0 mode is also known as the TEM mode. $\psi_{m+}(x,z)$ and $\psi_{m-}(x,z)$

represent modes traveling in the positive z-direction and the negative z-direction respectively.

Again the method of moments solution is used, but in this structure the fields have to be matched at several boundaries. The number of boundaries depends on the size of the groove and the length of the waveguide sections. Although these extra boundaries appear to complicate things, the fact that the potential functions are simple trigonometric expressions makes the computation a lot faster.

A simple matrix equation relates the coefficients of the fields in one waveguide section those in the adjacent waveguide section as

$$\begin{pmatrix} V & V \\ Y_1 & -Y_1 \end{pmatrix} \begin{pmatrix} a_i \\ b_i \end{pmatrix} = \begin{pmatrix} I & I \\ -V^T Y_2 & V^T Y_2 \end{pmatrix} \begin{pmatrix} a_{i+1} \\ b_{i+1} \end{pmatrix} \tag{5.19}$$

where the elements of the matrix $\mathbf{V}$ are given by the scalar product of the tangential fields at the interface, and the elements of the diagonal matrices $\mathbf{Y_1}$ and $\mathbf{Y_2}$ are the impedances of the individual waveguide modes. $\mathbf{I}$ is the unit matrix. a and b represent the coefficients of the modes traveling in the positive z-direction and the negative z-direction respectively. The upper half of this matrix equation is the boundary condition for the tangential electric field and the lower half the boundary condition for the tangential magnetic field.

The fields in air are connected to the fields in the last waveguide section by a similar matrix equation. By multiplying the matrices together, the coefficients of the fields in the first waveguide section (the one closest to the apex of the groove) are related to the coefficients of the fields in air through a set of linear equations. Now the first waveguide section is shorted at the end so that the coefficient of the wave traveling in the positive z-direction and the coefficient of the wave traveling in the negative z-direction of each mode are equal and opposite at the short. Using this boundary condition, one may find either the coefficients

of the reflected fields or the coefficients of the fields inside the groove. In this work one is interested in the fields inside the groove.

Results and Discussion.

The position of the antenna inside the groove, the dimensions of the groove, the elemental radiation pattern and the coupling efficiency are the parameters one has to consider in this design. The radiation resistance, which is strongly dependent on the type of antenna, is also an important parameter in designing an efficient imaging array. But in this section all the feed antennas are linearly polarized infinitesimal dipoles. Only estimates for the radiation resistance of these antennas are given.

In this design the antenna will be placed along the bisection CO of the groove. The fields along this line have to be known to find the position at which the antenna is to be placed. The larger the fields greater will the radiation resistance be. But this is not the only criterion for the vertical position. One has to be able to build a membrane on a mechanically stable and rigid piece of silicon. Furthermore the size of the membrane will depend on its vertical position. For fabrication purposes one would like the membrane to be small. Results shown below were all obtained using the stepped waveguide method. Identical results were obtained using the cylindrical wave function method indicating that the stepped waveguide method is extremely accurate. The results from the cylindrical wave function method were coincident with these curves and therefore not shown here. The formulas for the Bessel functions were obtained from Abramowitz and Stegun [37].

Fig. 5.6 shows the electric fields along CO for grooves of different sizes with a plane wave incident normal to the horn apertures. Fig. 5.6(a) is for polarization perpendicular to the grooves and Fig. 5.6(b) is for polarization parallel to the

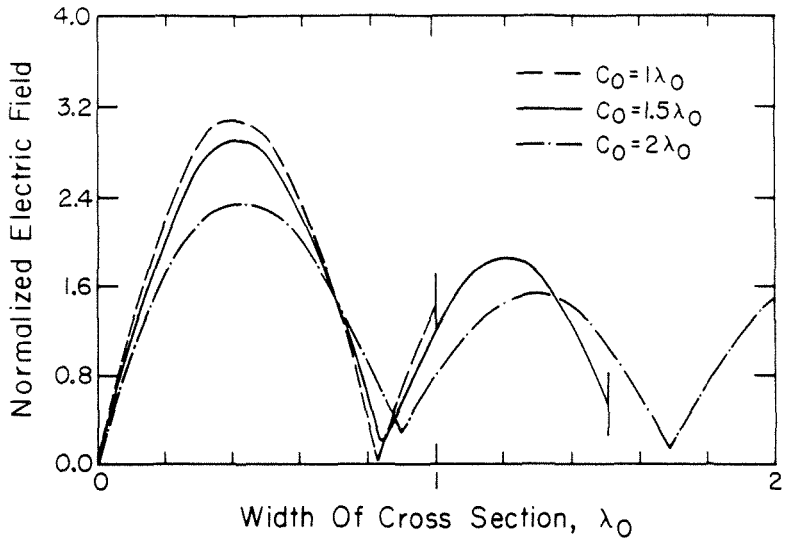

(a)

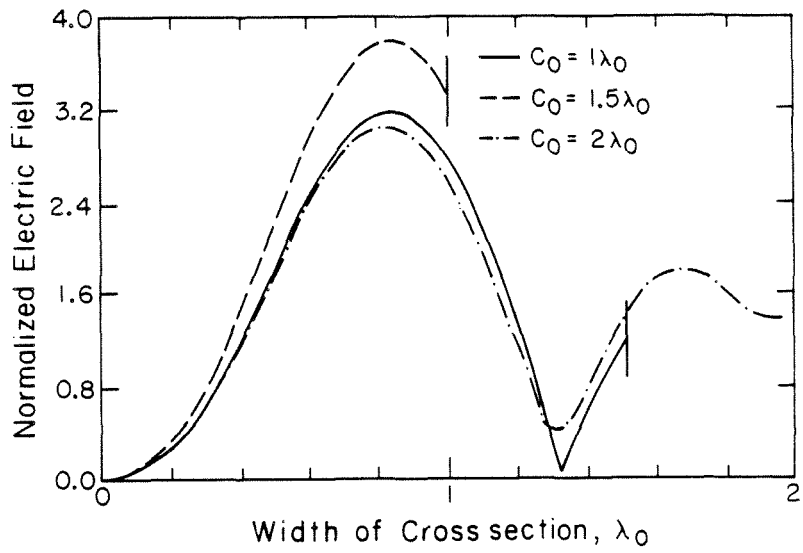

(b)

Figure 5.6 Fields along the horn bisection for (a) polarization perpendicular to the groove and (b) polarization parallel to the groove. c_0 is the aperture size.

grooves. In both cases the incident radiation seems to focus at a fixed distance from the apex of the groove. For the perpendicular polarization focusing occurs at a cross-section of about $0.4\lambda_0$ and for the parallel polarization it occurs at about $0.8\lambda_0$. This distance is independent of the groove size because near the

apex the power is carried mainly by the lowest order mode. Therefore the goal is to couple efficiently to these lowest order mode so as to get a reasonable radiation resistance and good coupling efficiency.

Fig. 5.7 shows the radiation patterns in the classical diffraction plane of these grooves for different groove spacing with the dipole placed at the point of maximum coupling. These patterns were found by calculating the fields at the position of the dipole in its absence. If the dipole is small and does not perturb the fields around it then by reciprocity the available power at the dipole is proportional to the square of the field. Fig. 5.7(a) shows the patterns for the perpendicular configuration. This figure shows that the radiation pattern of the $c_0 = 1.5\lambda_0$ is worse than that of $c_0 = \lambda_0$. But the third curve shows that one may obtain a better radiation pattern with the former if the dipole was moved to another position – at a cross-section of $1.1\lambda_0$. Therefore the point of maximum coupling is not necessarily the point which gives the best radiation pattern. Fig. 5.7(b) shows that the patterns of the parallel configuration is better behaved and steadily improve with increased groove spacing. The reason for this improvement is, in the latter case the electric fields taper off to zero at the edges of the grooves. Therefore the radiation pattern which is the Fourier transform of the aperture illumination is well behaved and has no side lobes. This is not true for the perpendicular configuration because the fields are normal to the groove edge and therefore not constrained to be zero. One way to improve this pattern is to introduce corrugations which make the groove walls look inductive thereby reducing the normal electric fields at the edge.

When the dipoles were placed at the nulls of the curves in Fig. 5.6 the patterns were broad and full of sidelobes. This is because at the nulls the fields are extremely sensitive to the changes in the incident angle, especially around

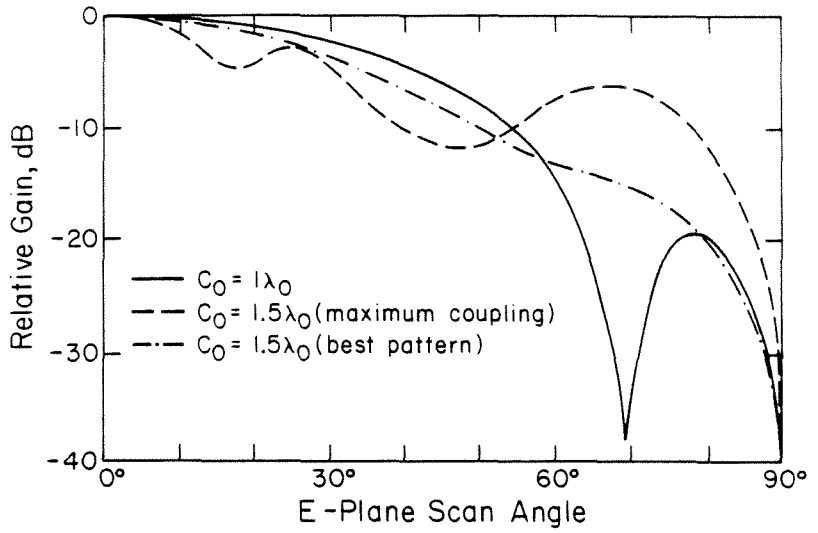

(a)

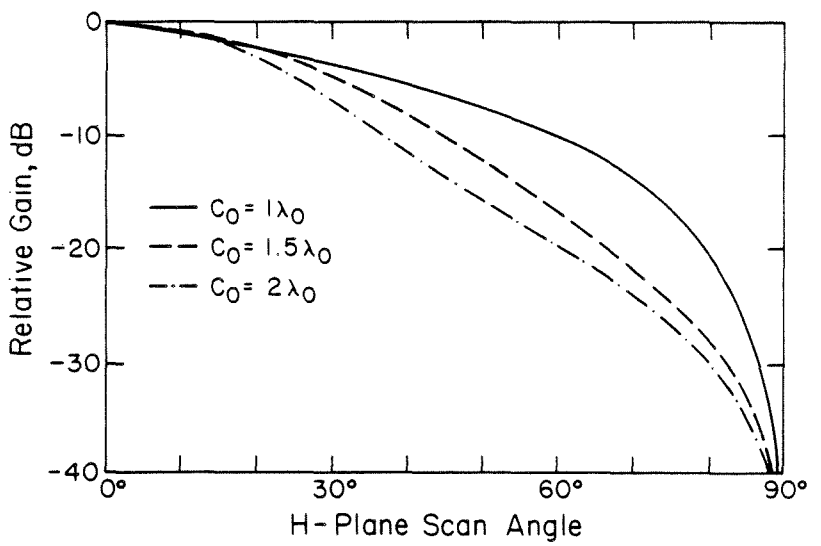

(b)

Figure 5.7 The radiation pattern in the classical diffraction plane, of grooves of different sizes for (a) the perpendicular dipole configuration and (b) the parallel dipole configuration. The dipoles were placed at the point where the fields were maximum except for the best pattern in (a) where the dipole was placed at a distance $1.1\lambda_0$ from the apex.

normal incidence. Finally if one was to build an imaging array consisting of parallel grooves it is clear from Fig. 5.7 that the parallel configuration is better suited. In this configuration the pattern in the plane along the groove will look like a cosine pattern resulting in good coupling efficiencies.

5.2 Two-Dimensional Pyramidal Horn Arrays.

The final design objective in this chapter was the two-dimensional pyramidal horn array. In the previous section, one-dimensional groove arrays were analyzed with the hope of being able to estimate the performance of pyramidal horn arrays. Horns have been studied extensively and their performance at RF and microwave frequencies have been documented [15]. But most of the standard analysis methods apply to large horns with small horn flare angles. In this design the horn-half angle is 35.3° and the horn aperture is of the order of a free space wavelength. The aim is to design an array where the horn dimensions and the dipole position are best suited to give optimum performance with a specific optical system.

The stepped waveguide method is again used to analyze pyramidal horns. For pyramidal horns, the horn is sectioned into small sections of rectangular waveguides as shown in Fig. 5.8. This method has been used before in the analysis of waveguide filters [38–39] and horns [35]. The coupling between rectangular waveguide sections of different sizes has been investigated thoroughly [40–42]. The advantage of this method is that one may use it to analyze simple horns of any flare angle and size as long as enough modes are taken and if the sectioning is such that it closely approximates the real pyramidal horn. Furthermore this method may be used to analyze corrugated horns too [35]. The horns in this design were assumed to have a square cross-section.

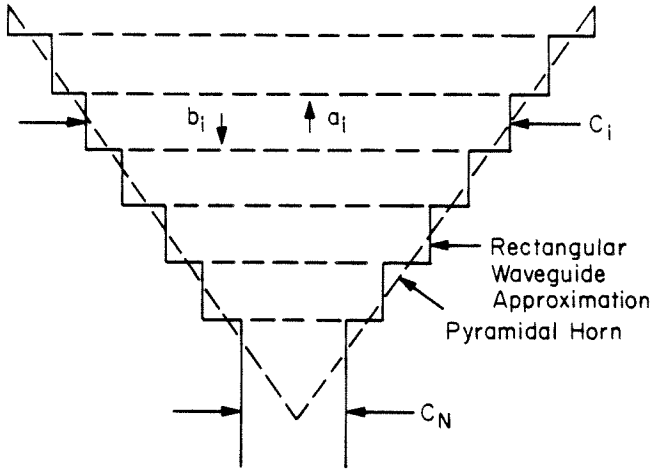

Figure 5.8 The stepped waveguide method for the pyramidal horn. Instead of a short at the apex a infinitely long rectangular waveguide section starting at a point at which the fields have decayed to some small value is added on at the end.

Analysis Using the Stepped Waveguide Method.

The analysis is similar to that of the previous section. The horn is approximated by a structure more suitable for numerical methods. The horn is sectioned into multiple rectangular waveguide sections and the fields in each section are given by a linear combination of the waveguide modes [36]. The fields in air are given by two-dimensional Floquet modes [23]. The method of solution is exactly the same as the previous section. The boundary conditions are matched at each of the waveguide discontinuities and at the aperture of the horn. The Galerkin method gives a set of linear equations which may be solved to give the field components.

The fields in the ith rectangular waveguide section is given by the potential function

$$F_1^i = \sum_{m=(0)1}^{\infty} \sum_{n=(0)1}^{\infty} (a_{mn}\psi^i_{mn+}(x,y,z) + b_{mn}\psi^i_{mn-}(x,y,z)), \qquad (5.20)$$

where

$$\Psi^i_{mn\pm}(x,y,z) = \frac{\sqrt{(2-\delta_{0m})(2-\delta_{0n})}}{c_i} f(k_m x)\, g(k_n y)\, exp(\mp j\gamma_{mn} z), \qquad (5.21)$$

$$k_m = \frac{m\pi}{c_i},$$

$$k_n = \frac{n\pi}{c_i},$$

$$\gamma_{mn} = \sqrt{k_0^2 - k_m^2 - k_n^2},$$

where $f(k_m x)$ and $g(k_n y)$ are simple sine or cosine functions and c_i the dimension of the waveguide wall.

Using the Galerkin method at every waveguide discontinuity one gets a set of linear equations like equation (5.19). In this case the diagonal matrices $\mathbf{Y_1}$ and $\mathbf{Y_2}$ are the impedances of the individual rectangular waveguide modes. Having written similar matrix equations for each waveguide discontinuity one combines them all into one matrix equation that relates the coefficients in the last section to the coefficients in the first section. The fields in air may be given by the potential

$$F_2 = \sum_{m=-\infty}^{\infty} \sum_{n=-\infty}^{\infty} (c_{mn}\, \phi_{mn+}(x,y,z) + d_{mn}\, \phi_{mn-}(x,y,z)), \qquad (5.22)$$

where

$$\phi_{mn\pm} = \frac{1}{c_0} exp - j(\alpha_m x + \beta_n y \pm \gamma_{mn} z), \qquad (5.23)$$

where

$$\alpha_m = \alpha_0 + \frac{2m\pi}{c_0},$$

$$\beta_n = \beta_0 + \frac{2n\pi}{c_0},$$

$$\gamma_{mn} = \sqrt{k_0^2 - \alpha_m^2 - \beta_n^2},$$

Again one may use the Galerkin method to get a matrix equation similar to equation (5.19) relating the coefficients in the last section to the coefficients in air.

In this analysis instead of taking the first section at the apex, it is taken to be a section which is not necessarily very small but small enough to have only rapidly decaying evanescent waves (Fig. 5.8). This section is assumed to be an infinite rectangular waveguide with waves only traveling in the negative z-direction. This is a reasonable assumption because the waves decay so fast that the reflected fields beyond this section are negligible. Unlike the parallel plate case, all the modes in the rectangular waveguide have finite cut-off points. The advantage of this method is that one does not have to deal with extremely small waveguide sections where the decay constants are large. Large decay constants tend to introduce large errors because they make the stepped waveguide approximation less accurate (smaller sections are required). Tests similar to those in the previous section were used to check the accuracy and the convergence of these solutions.

Results and Discussion.

A program was written to calculate the fields inside the horn for plane waves incident at different angles of incidence. To illustrate the effect of the flare angle the radiation pattern was calculated for a waveguide coupled horn of aperture size $1\lambda_0$ for different flare angles. Figs. 5.9(a) and 5.9(b) show these radiation patterns in the E-plane and the H-plane respectively. The patterns were calculated for horn half-angles of 10°, 20° and 30°. The E-plane patterns clearly degrade fast when the flare angle is increased. But the H-plane pattern is not very sensitive to the flare angle. In this design the horn half-angle is 35.3°. Therefore the E-plane patterns will look somewhat like the large angle patterns in Fig. 5.9(a). The coupling between the different modes in a horn element was

found to increase with the flare angle. This is one of the reasons why conventional analysis techniques fail for large angle horns. Coupling between horn elements was observed for horn sizes smaller than $1\lambda_0$.

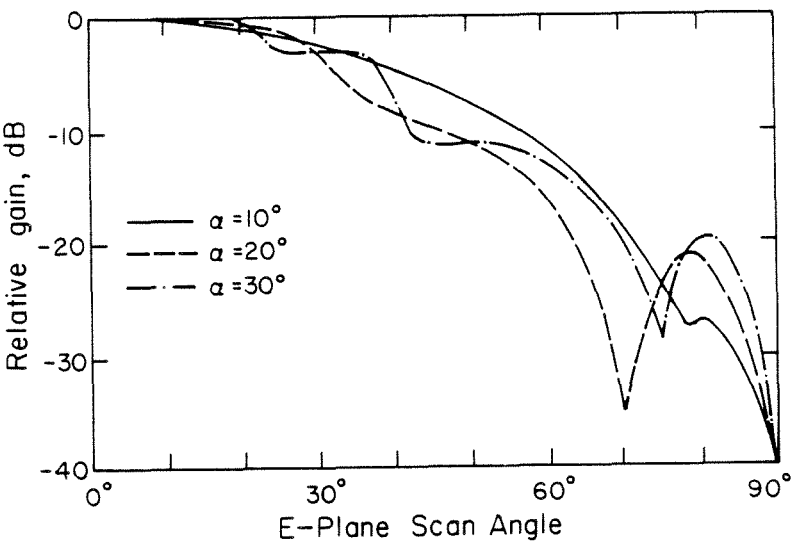

(a)

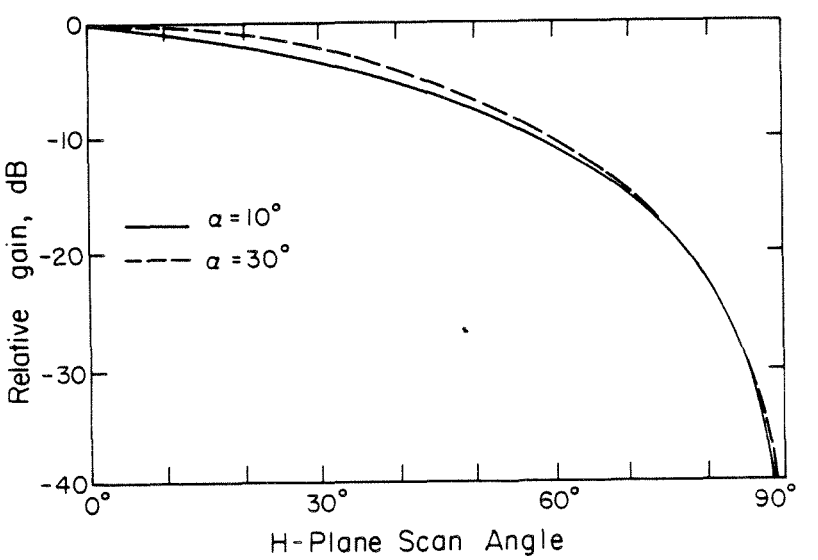

(b)

Figure 5.9 The radiation patterns of a waveguide-fed horn of aperture size $1\lambda_0$. (a) shows the E-plane patterns and (b) shows the H-plane patterns.

In all the other calculations it was assumed that the horn was excited by an infinitesimal dipole which does not perturb the fields inside the horn. The position of the dipole not only determines the radiation resistance but it also determines the size of the membrane. Fig. 5.10 shows the normalized electric fields along the horn axis plotted for horns of different aperture sizes. Again like the groove array the fields seem to focus at some fixed point. In this case this focus was at a cross-section of about $0.8\lambda_0$. For a horn array with aperture size of $1\lambda_0$ this would mean that the dipole (and the membrane) will be very close to the horn aperture, making the structure mechanically unstable. One suitable solution is to build the membrane deeper at the expense of lower radiation resistance. One would prefer to get around this by using a larger horn size.

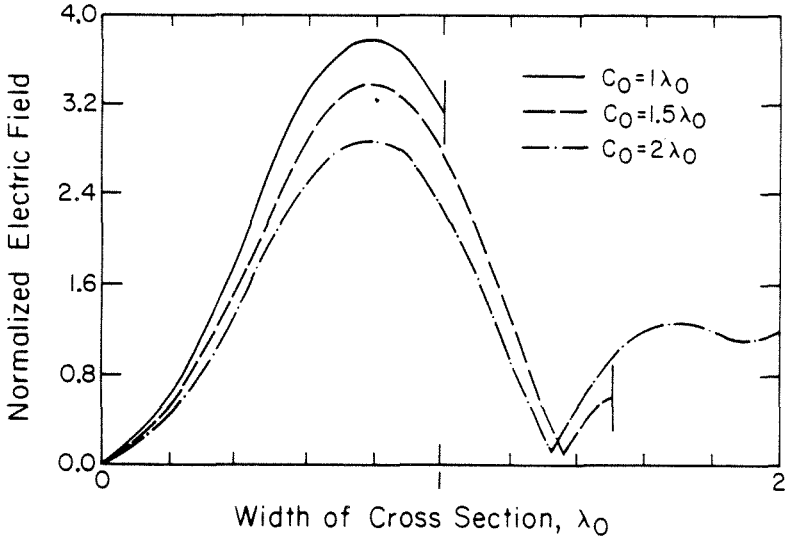

Figure 5.10 Fields inside the horn along the horn axis for different horn sizes.

Figs 5.11, 5.12 and 5.13 show the E-plane and H-plane radiation patterns of horns of different aperture sizes. The H-plane pattern is well behaved for horns of most sizes. But the E-plane pattern has side lobes. Larger horns have more side lobes in the E-plane than smaller horns. Again this is due to the pattern being the Fourier transform of the aperture illumination. Therefore, when the

horn aperture size is increased, the side lobes get closer together. An interesting observation in calculating the radiation pattern of the pyramidal horns was that, unlike the patterns of the grooves with perpendicular dipoles, these patterns were not very sensitive to the position of the dipole inside the horn. This is because in the pyramidal horn all the modes are evanescent beyond a cross-section of $0.5\lambda_0$, while in the groove power travels all the way to the apex of the groove and reflects back. Therefore the effect on the pattern due to higher order modes is greater in the latter, resulting in a greater sensitivity to the dipole position.

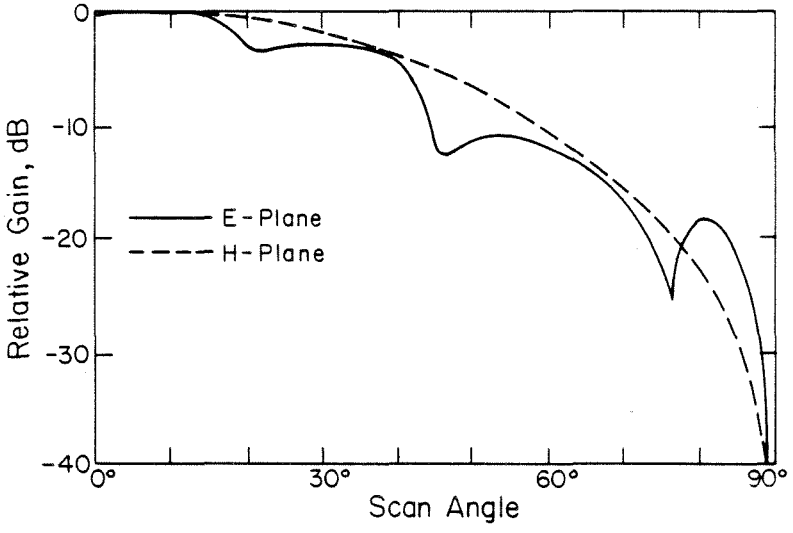

Figure 5.11 The E-plane and H-plane elemental radiation patterns of a pyramidal horn in an infinite array. The aperture size $c_0 = 1\lambda_0$.

Fig. 5.14 shows the coupling efficiencies of a horn element in a two-dimensional array plotted against the $f_{\#}$. The aperture size is $1.5\lambda_0$. The figure also shows the spillover loss and the taper loss. The coupling efficiency peaks around 60% for a $f_{\#}$ of about 0.75. If one is to use this horn array for diffraction limited imaging then the $f_{\#}$ has to be greater than 1.5. The efficiency at this $f_{\#}$ is

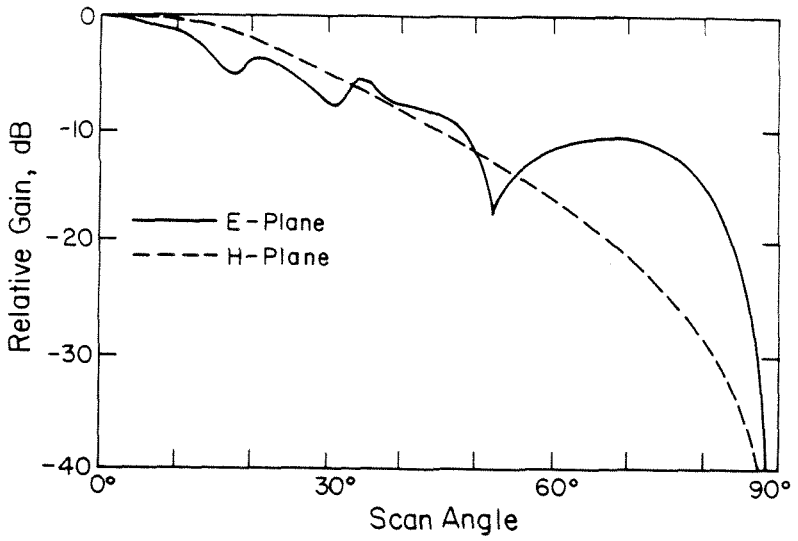

Figure 5.12 The E-plane and H-plane elemental radiation patterns of a pyramidal horn in an infinite array. The aperture size $c_0 = 1.5\lambda_0$.

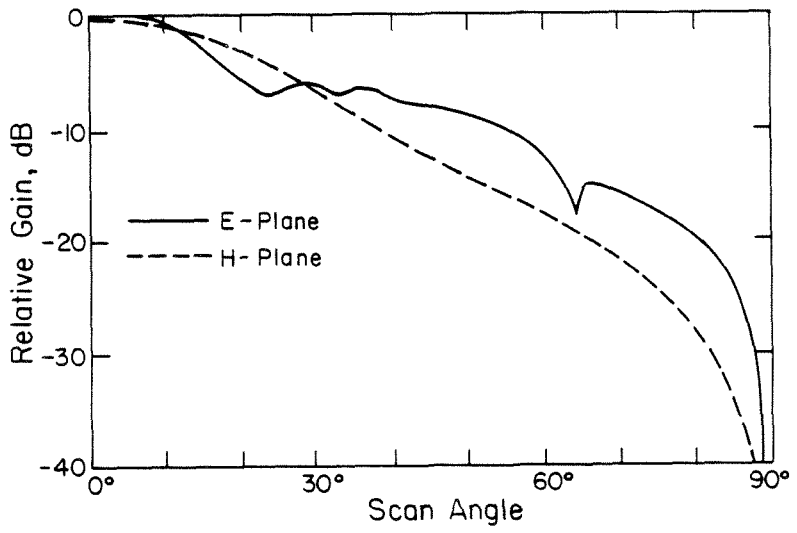

Figure 5.13 The E-plane and H-plane elemental radiation patterns of a pyramidal horn in an infinite array. The aperture size $c_0 = 2\lambda_0$.

about 40% which is still very good. The broad maximum in this curve allows some flexibility in designing a diffraction limited imaging array.

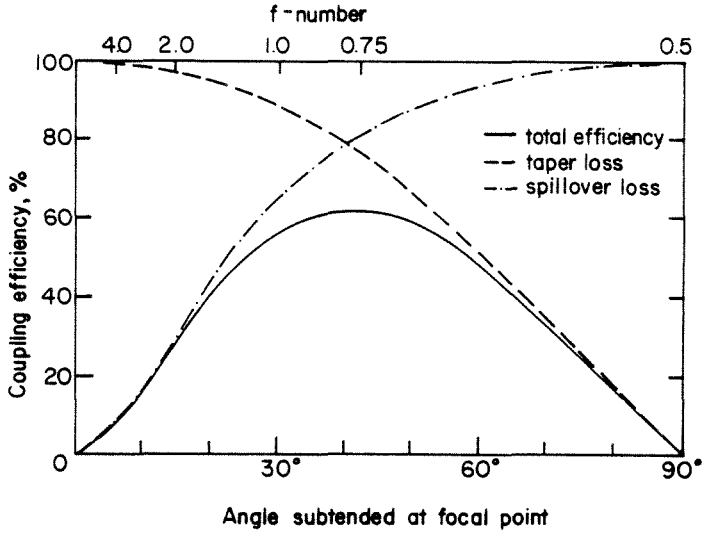

Figure 5.14 The coupling efficiency of a horn element in an infinite array. The horn aperture size is $1.5\lambda_0$ and the dipole is placed at a distance $0.6\lambda_0$ from the apex. The efficiency calculations are from [13].

Horns with larger apertures have better radiation patterns. But larger horns require large $f_{\#}$'s (equation (5.4)) to achieve diffraction limited imaging. This would mean a degradation in the intrinsic resolution of the optical system. Therefore the optimum size would be something in between. The improvement in the patterns between $c_0 = 2\lambda_0$ and $c_0 = 1.5\lambda_0$ is small compared to the improvement between the latter and $c_0 = 1\lambda_0$. This would suggest that the most suitable design would be to use an array with horns of the size $1.5\lambda_0$ in an optical system with $f/1.5$. The $f/1.5$ optical system provides high resolution along with reasonably aberration-free imaging.

The most suitable position for the membrane is at the point where the electric fields are the highest, $0.6\lambda_0$ from the apex. At this point the dipole will have the

highest radiation resistance. This point is sufficiently deep inside the horn to be able to use a small membrane. The membrane size would be about $0.8\lambda_0$, which at 94GHz would be about 2.5mm. A membrane of this size can be fabricated and would have good mechanical strength.

The elemental gain of the above horn was found to be about 13dB. This translates to an effective area of about $1.5\lambda_0^2$. Therefore the aperture efficiency is about 67%. These numbers are very promising considering that the horn's aperture is small. The impedance of the infinitesimal dipole was found to be about $70\pi^2\,(h/\lambda_0)^2$. If one compares this with $80\pi^2\,(h/\lambda_0)^2$, which is the impedance of the same dipole in free space, and assuming that one may extrapolate to finite length dipoles, one would expect an impedance of about 64Ω for a quarter-wave dipole.

5.3 Conclusion.

It has been shown that small horns with aperture sizes comparable with the free space wavelength coupled with dipole antennas may be used as feed antennas in diffraction limited imaging systems. The groove arrays when coupled to a parallel dipole may also be used either as a one-dimensional imaging array or as a two-dimensional imaging array. The radiation patterns of these horns and grooves were very well behaved in the H-plane, but the patterns in the E-plane had sidelobes. A two-dimensional array consisting of pyramidal horns of aperture size $1.5\lambda_0$ was suggested as a possible design with an $f/1.5$ optical system. The elemental gain of these horns was shown to be about 13dB with a aperture efficiency of around 67%. The impedance of a quarter-wave dipole inside this horn was estimated to be around 64Ω.

References.

[1] D. P. Neikirk *et al.*, "Far-Infrared Imaging Antenna Arrays," *Appl. Phys. Lett.*, **40**, pp. 203-205, 1982.

[2] P. P. Tong *et al.*, "Tracking Antenna Array for Near-Millimeter-Waves," *IEEE Trans. Antennas Propagat.*, **AP-31**, pp. 512-515, 1983.

[3] P. E. Young *et al.*, "Multichannel Far-Infrared Phase Imaging for Fusion Plasmas," *Rev. Sci. Instrumen.*, **56**, pp. 81–89, 1985.

[4] P. F. Goldsmith, "Quasi-Optical Techniques at Millimeter and Submillimeter Wavelengths," *Infrared and Millimeter Waves*, **6**, pp. 277-343, K. J. Button ed., Academic Press Inc., 1982.

[5] P. J. B. Clarricoats, G. T. Poulton, "High-Efficiency Microwave Reflector Antennas – A Review," *Proc. IEEE*, **65**, pp. 1470–1504, 1977.

[6] R. S. Elliott, *Antenna Theory and Design*, Prentice-Hall Inc., pp. 482–556, 1981.

[7] C. A. Balanis, *Antenna Theory*, Harper and Row, New York, pp. 593–657, 1982.

[8] K. S. Yngvesson, "Near-Millimeter Imaging with Integrated Planar Receptors," *Infrared and Millimeter Waves*, **10**, pp. 91–110, K. J. Button ed., Academic Press Inc., 1983.

[9] D. P. Rutledge, M. S. Muha, "Imaging Antenna Arrays," *IEEE Trans. Antennas Propagat.*, **AP-30**, pp. 535–540, 1982.

[10] C. R. Brewiit-Taylor *et al.*, "Planar Antennas on a Dielectric Surface," *Electron. Lett.*, **12**, pp. 729–731, 1981.

[11] R. C. Compton, G. M. Rebeiz, D. B. Rutledge, "Developments in Two-Dimensional Arrays," *10th Intl. Conf. on Infrared and Millimeter Waves*, pp. 277-278, 1985.

[12] S. E. Schwarz, "Efficiency of Quasi-Optical Couplers," *Intl. J. Infrared and Millimeter Waves*, **5**, pp. 1517–1525, 1984.

[13] C. E. Zah, R. C. Compton, D. B. Rutledge, "Efficiencies of Elementary Integrated Circuit Antennas," *Electromagnetics*, **3**, pp. 239–254, 1983.

[14] G. M. Rebeiz *et al.*, "Submillimeter-Wave Antennas on Thin Membranes," 11th. Intl. Conf. on Infrared and Millimeter Waves, pp. 694–696, 1986.

[15] A. W. Love, *Electromagnetic Horn Antennas*, IEEE Press, New York, 1976.

[16] A. W. Rudge *et al.*, "Design of Flared-Horn Primary Feeds for Parabolic Reflector Antennas," *Proc. IEE*, **117**, pp. 1741–1749, 1970.

[17] P. M. Russo *et al.*, "A Method of Computing E-Plane Patterns of Horn Antennas," *IEEE Trans. Antennas Propagat.*, **AP-13**, pp. 219–224, 1965.

[18] J. S. Yu, R. C. Ruddock, L. Peters, "Comprehensive Analysis for E-Plane of Horn Antennas by Edge-Diffraction Theory," *IEEE Trans. Antennas Propagat.*, **AP-14**, pp. 138–149, 1966.

[19] N. Amitay, M. J. Gans, "Design of Rectangular Horn Arrays with Oversized Aperture Elements," *IEEE Trans. Antennas Propagat.*, **AP-29**, pp. 871–884, 1981.

[20] V. Galindo, C. P. Wu, "Numerical Solutions for an Infinite Phased Array of Rectangular Waveguides with Thick Walls," *IEEE Trans. Antennas Propagat.*, **AP-14**, pp. 149–158, 1966.

[21] C. P. Wu, V. Galindo, "Properties of a Phased Array of Rectangular Waveguides with Thin Walls," *IEEE Trans. Antennas Propagat.*, **AP-14**, pp. 163–172, 1966.

[22] N. Amitay, V. Galindo, C. P. Wu, *Theory and Analysis of Phased Array Antennas*, John Wiley and Sons, New York, 1972.

[23] R. C. McPhedran *et al.*, "Theory of Crossed Gratings," *Electromagnetic*

Theory of Gratings, R. Petit ed., Springer-Verlag, New York, pp. 227–276, 1980.

[24] J. W. Goodman, *Introduction to Fourier Optics*, McGraw-Hill, New York, pp. 48–54, 1968.

[25] M. Born, E. Wolf, *Principles of Optics*, Pergamon Press, Oxford, pp. 484, 1980.

[26] D. B. Rutledge, S. E. Schwarz, "Planar Multimode Detector Arrays for Infrared and Millimeter-Wave Applications," *IEEE J. Quantum Electron.*, **QE-17**, pp. 407-414, 1981.

[27] Y. Obha, "On the Radiation of a Corner Reflector Finite in Width," *IEEE Trans. Antenna Propagat.*, **AP-11**, pp. 127-132, 1963.

[28] R. M. Finne, D. L. Klein, "A Water-Amine-Complexing Agent System for Etching Silicon, *J. Electrochem. Soc.*, *114*, pp. 965–970, 1967.

[29] R. F. Harrington, *Time Harmonic Electromagnetic Waves*, McGraw-Hill, New York, 1961.

[30] J. W. S. Rayleigh, *Proc. Royal Soc.*, **A 79**, pp. 399, 1907.

[31] D. Maystre, "Integral Methods," *Electromagnetic Theory of Gratings*, R. Petit ed., Springer-Verlag ed., New York, pp. 63–100, 1980.

[32] R. F. Harrington, *Field Computation by Moment Methods*, Macmillan and Sons, New York, 1968.

[33] R. Mittra, C. A. Klein, "Stability and Convergence of Moment Method Solutions," *Numerical and Asymptotic Techniques in Electromagnetics*, R. Mittra ed., Springer-Verlag, New York, 1975.

[34] K. T. Lee, T. F. George, "Theoretical Study of Laser-Induced Excitations on a Grating," *Phys. Rev.*, **31**, pp. 5106–5112, 1985.

[35] J. A. Encinar, J. M. Rebollar, "A Hybrid Technique for Analyzing Cor-

rugated and Noncorrugated Rectangular Horns," *IEEE Trans. Antennas Propagat.*, **AP-34**, pp. 961-968, 1986.

[36] R. E. Collin, *Field Theory of Guided Waves*, McGraw-Hill, New York, 1960.

[37] M. Abramowitz, I. Stegun, *A Handbook of Mathematical Functions*, Dover Publications, New York, 1964.

[38] H. Patzelt, F. Arndt, "Double-Plane Steps in Rectangular Waveguides and their Application for Transformers, Irises, and Filters," *IEEE Trans. Microwave Theory Tech.*, **MTT-30**, pp. 771–776, 1982.

[39] G. Matthaei, L. Young, E. M. T. Jones, *Microwave Filters, Impedance-Matching Networks and Coupling Structures*, McGraw-Hill, New York, 1964.

[40] A. Wexler, "Solution of Waveguide Discontinuities by Modal Analysis," *IEEE Trans. Microwave Theory Tech.*, **MTT-15**, pp. 508–517, 1967.

[41] R. Safavi-Naini, R. M. MacPhie, "Scattering at Rectangular-to-Rectangular Waveguide Junctions," *IEEE Trans. Microwave Theory Tech.*, **MTT-30**, pp. 2060–2063, 1982.

[42] Y. C. Shih, K. G. Gray, "Convergence of Numerical Solutions of Step-Type Waveguide Discontinuity Problems by Modal Analysis," *Intl. Microwave Symp.*, Boston, Massachussetts, 1983.

CHAPTER 6.

Future Work in Millimeter-Wave Imaging Arrays.

In this thesis I have looked at two different ways of achieving diffraction limited imaging at millimeter-wave frequencies. The first method uses a substrate lens-coupled imaging system [1]. The other is a two-dimensional array of small horns. There is more work to be done in both of these projects. This includes the implementation of these designs and also improvements to them.

The lens-coupled array requires some work into the proper implementation of the design. The lenses have to be small and be of optical quality material. Wengler *et al.* [2] have used small quartz lenses before in their near-millimeter SIS junction receivers. The lens in their receiver had a diameter of about 3.3mm. Recent work [3–4] on material processing techniques makes the fabrication of smaller lenses more viable. This design could get a major boost if it is possible to monolithically fabricate such an array of small lenses. Work along these lines is being done at Corning [5].

The biggest drawback of lens-coupled systems is that the lens degrades the radiation pattern of the feed antennas. However good the feed antenna is, it is impossible to get good radiation patterns from lens coupled systems. One possible improvement is to use stratified lenses of different dielectric constants. Another method would be to synthesize patterns using layers of dielectric substrates [6]. If one judiciously selects the dielectric materials and their thicknesses, it is possible to synthesize a reasonable radiation pattern. This design will also suppress substrate-modes if it is built like a impedance transformer. It will still have the advantage of radiating mainly into the dielectric side, which improves the gain and the coupling efficiency.

The second imaging array consisting of pyramidal horns requires some work in the fabrication process. Although log-periodic antennas have been built successfully on thin membranes [7] the extension of this to the pyramidal horn requires further development. This would mean developing ways of building horn elements which are about a wavelength in size and aligning the horn elements with their backshorts. One may also think of making corrugations inside the horn to improve the E-plane pattern. Another possibility is to develop new etching techniques that will result in smaller horn angles. This would enhance the patterns considerably and improve the coupling efficiency.

There is room for improvement in the membrane fabrication. Currently in the integrated-circuits laboratory it possible to make membranes up to 3mm in size. One would like to be able to build larger membranes with the hope of working at lower frequencies like 60 GHz. This would require development work in the material processing techniques. It may also be possible to build thin silicon supports for the membranes. This would allow one to use the existing membranes in larger apertures. Another possible improvement to this project would be to build arrays on GaAs. One may think of using GaAs membranes also. This would allow one to build Schottky diode detectors on the membrane and achieve coherent detection.

Furthermore, as these arrays are free standing in air, they may be also used as phased arrays at millimeter-wave frequencies [8]. Considerable amount of work is going on in developing efficient phase shifters and beam steering equipment [9] at millimeter-wave frequencies. The horns in the phased array will have to placed much closer together. This is because of the grating lobes. The element spacing will have to be smaller than a wavelength if one hopes to avoid grating lobes. But as the horn pattern is reasonably directed even at an aperture size of

$1\lambda_0$, it is possible to make a good phased array with these horns. One might be limited to small scan angles though.

Finally, these horns may be used even at submillimeter-wave frequencies [7]. Problems may arise due to small wafer sizes when the frequencies are greater than 700 GHz. But by using large $f_{\#}$ systems, one may be able to push this limit to around the 1 THz mark. As microbolometers perform well at these frequencies one should consider using them for these designs.

References.

[1] D. P. Kasilingam, D. B. Rutledge, "Focusing Properties of Small Lenses," *Intl. J. of Infrared and Millimeter Waves*, **7**, pp. 1631–1648, 1986.

[2] M. J. Wengler *et al.*, "A Low Noise Receiver for Millimeter and Submillimeter Wavelengths," *Intl. J. of Infrared and Millimeter Waves*, **6**, pp. 689–696, 1985.

[3] Y. S. Lau, D. Nicholson, "Barium Ferrite Tuned-Indium Phosphide Gunn Millimeter Wave Oscillators," *Intl. Microwave Symp.*, pp. 183, 1986.

[4] K. D. Wise, "Silicon Micromachining and its Application to High Performance Integrated Sensors," *Micromachining and Micropackaging of Transducers*, Elsevier, New York, 1985.

[5] N. P. Borrelli *et al.*, "Photolytic Technique for Producing Microlenses in Photosensitive Glass," *Appl. Optics*, **24**, pp. 2520–2525, 1985.

[6] N. G. Alexopoulos *et al.*, "Substrate Optimization for Integrated Circuit Antennas," *IEEE Trans. Microwave Theory Tech.*, **MTT-31**, pp. 550–557, 1983.

[7] G. M. Rebeiz *et al.*, "Submillimeter-Wave Antennas on Thin Membranes," 11th. Intl. Conf. on Infrared and Millimeter Waves, 1986.

[8] G. M. Rebeiz, *Private communication.*

[9] W. M. Lam *et al.*, "Diode Grids for Electronic Beam Steering and Frequency Multiplication," *Intl. J. of Infrared and Millimeter Waves*, **7**, pp. 27–41, 1986.

APPENDIX

Analysis of Schottky Barrier Diode Mixer Circuits.

Schottky diode mixers have been used extensively in millimeter-wave receivers [1–3] and imaging arrays [4]. The GaAs Schottky diode is especially suited for millimeter-wave systems because of its low capacitance and series resistance. Different varieties of Schottky diodes have been used in receivers up to 300 GHz [3] with single side band conversion losses of about 6 dB. Most previous diodes have been of the point contact variety. But in recent times with the advent of monolithic circuits, considerable research has gone into making high performance planar Schottky diodes for integrated circuits [4]. The work presented in this appendix is an analysis of Schottky diode heterodyne mixer circuits with subsequent optimization of mixer circuit design.

The analysis is based on an excellent piece of work analyzing the performance of Schottky diode mixer circuits by Held and Kerr [5]. Some of this work was presented in the doctoral thesis of Peter Siegel [6]. In their analysis Held and Kerr use an equivalent circuit consisting of the intrinsic diode, the series resistance and stray capacitance, and a frequency dependent embedding network as shown in Fig. A.1. The embedding network consists of all circuit elements external to the diode like the transmission lines, the antenna and the waveguide feed. The analysis constitutes of two sections. First the effect of the local oscillator is determined in the large signal analysis [7]. In this section the voltage, current, capacitance and conductance waveforms of the diode are generated and the Fourier series components of these waveforms are calculated. Next, the signal is introduced as a linear perturbation on the existing large signal environment. In this section the mixer is modeled by a linear multi-port network with each port

representing a side band frequency [8]. The small signal analysis predicts the performance of the mixer circuit by calculating the single side band conversion loss and the noise temperature of the mixer.

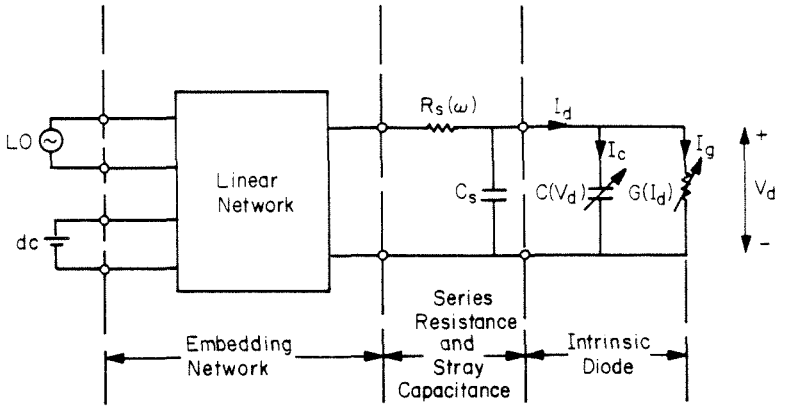

Figure A.1 The equivalent circuit of a single diode mixer (from Siegel [6]).

A program based on Held and Kerr's model was written to analyze mixer circuits. In this appendix, I present results to show how different circuit parameters and diode parameters influence the performance of the mixer. The diode parameters here are the series resistance, the zero bias capacitance, the stray capacitance and the diode temperature. The circuit parameters are the embedding impedances at the different side band frequencies, the bias voltage and the local oscillator power. Certain parameters effect the conversion loss and others the noise temperature. But in most cases the effects on the conversion loss and the noise temperature are similar. Finally this program is used to simulate the heterodyne detection process in the GaAs Schottky diode imaging array developed by my colleague Chung-en Zah [4,9].

A.1 Simulation of Schottky Diode Mixer Circuits.

The simulation program consists of two subroutines for the large signal analysis and the small signal analysis. The values of the embedding impedance at all

the side band frequencies have to be predetermined and stored in a data file. The program begins with tables showing the default values of the circuit parameters and the diode parameters. These values may be changed to suit a given diode at any operating condition. Having adjusted all the parameters, the program is then run to calculate the large signal Fourier coefficients. Fig. A.2 shows the simulated voltage and current waveforms of Zah's diode [4] over a local oscillator cycle. The Fourier coefficients are also calculated for the conductance and the capacitance of the diode. These values are required in the small signal analysis to find the incremental change in voltage and current.

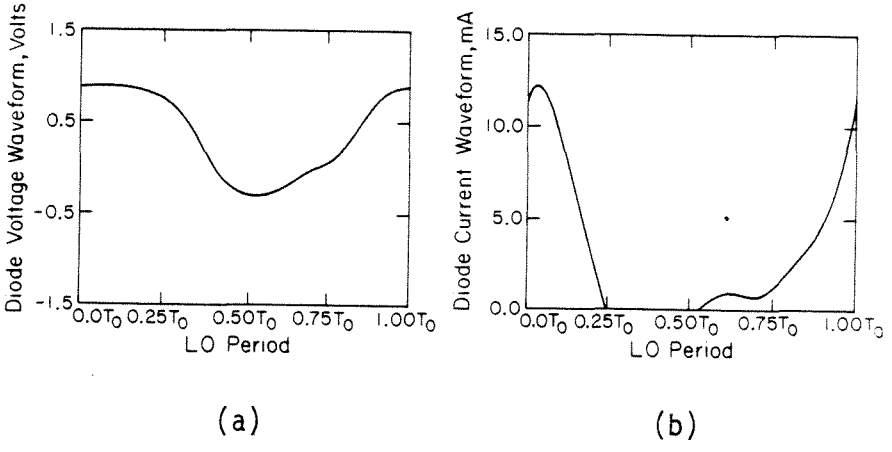

Figure A.2 (a) The diode voltage waveform and (b) the current waveform over a local oscillator period.

Having calculated the Fourier coefficients from the large signal analysis the small signal analysis routine then calculates the power received at the intermediate frequency (IF) for a given input signal (RF). The conversion loss is defined as the ratio of the power delivered at the IF frequency to the power in at the RF frequency. The single side band (SSB) conversion loss is calculated by taking into consideration the power in the IF signal side band, while the double side band (DSB) case takes both the signal and the image side band power into con-

sideration. In most cases the DSB conversion loss is less than the SSB conversion loss by approximately 3dB.

The noise analysis calculates the contributions of the shot noise and the thermal noise at the IF frequency. A good analysis of the noise mechanisms in resistive diodes is given by Dragone [10]. In his work Siegel [6] shows that the shot noise in the different ports are correlated while the thermal noise is uncorrelated. The thermal noise is due to the series resistance of the diode and is zero for a purely resistive mixer [11] which has zero series resistance and capacitance. The noise temperature is defined as the temperature of a ideal noise generator at the input of the mixer circuit needed to produce an equivalent amount of noise power at the output. The noise figure is related to the noise temperature by,

$$F = 1 + \frac{T_N}{T_0}, \tag{A.1}$$

where F is the noise figure, T_N the mixer noise temperature and T_0 the ambient temperature.

A.2 Results and Discussion.

The diode conductance is given by,

$$g_d = \alpha I_s \, exp(\alpha V_d), \tag{A.2}$$

where α is a number dependent on the diode doping and temperature, I_s is the saturation current which also depends on the temperature and V_d is the diode voltage. It is this non-linear conductance that causes mixing, which results in power being transferred to the side band frequencies. Therefore ideally one would like this non-linear conductance to be large. In frequency multipliers the non-linear junction capacitance is used to generate harmonics [6,12].

The conversion loss was determined for Zah's diode while varying different circuit parameters and diode parameters. Figs. A.3 to A.7 show the conversion loss plotted against the zero-bias capacitance, the stray capacitance, the series resistance, the local oscillator power and the bias voltage respectively. The noise temperature showed similar dependence on these parameters, except its dependence on the series resistance and the diode temperature were stronger.

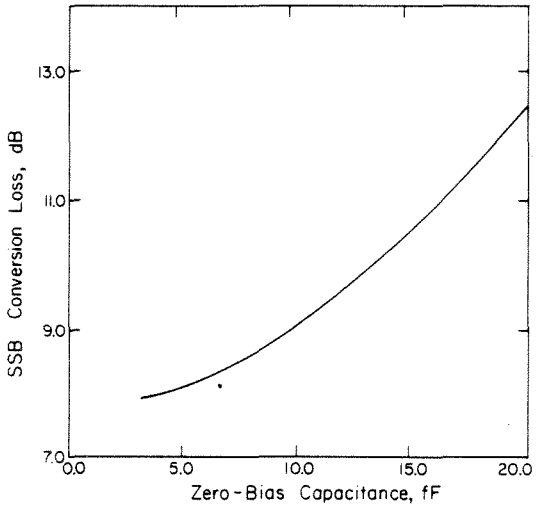

Figure A.3 Conversion loss *vs.* zero-bias capacitance for Zah's diode.

Figs A.3 and A.4 show that by increasing either the zero-bias capacitance or the stray capacitance of the diode the mixer performance may be degraded. This is to be expected as the increase in the capacitance results in less efficient transfer of power due to the phase difference. The series resistance will have a similar effect (Fig. A.5). In this case the series resistance increases the loss in the mixer circuit by dissipating power. The increase in thermal noise due to the series resistance makes the noise temperature strongly dependent on the former. For above-mentioned reasons, one of the objectives of Schottky diode designers is to try and minimize the series resistance and the capacitances of the diode [13].

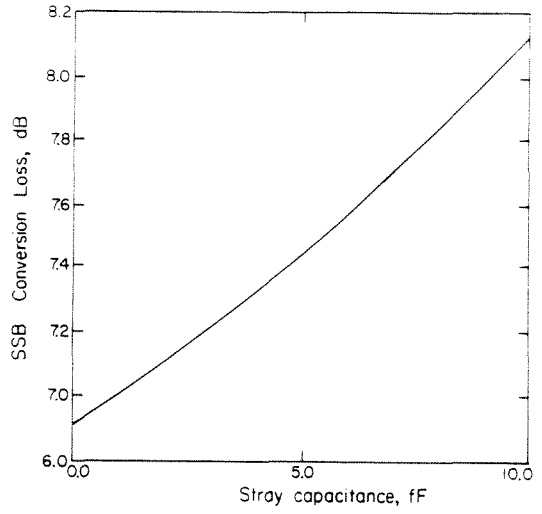

Figure A.4 Conversion Loss *vs.* stray capacitance for Zah's diode.

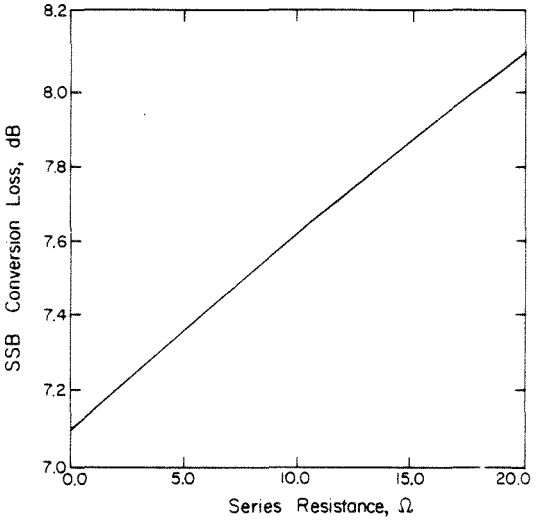

Figure A.5 Conversion loss *vs.* series resistance of Zah's diode.

The conversion loss was found to increase with the diode temperature, but the dependence was very slight. The diode temperature had to change considerably to show significant changes in the conversion loss. The noise temperature, on the other hand, showed a strong dependence on the diode temperature. This is because the thermal noise power generated by the series resistance is directly

proportionate to the diode temperature.

Fig. A.6 shows that by increasing the bias voltage the conversion loss may be reduced. In fact this dependence on the bias voltage is quite strong especially at low bias voltages. This is due to the diode having a finite turn on voltage below which the diode non-linear conductance is negligibly small. The diode must operate in the non-linear region to have good mixer performance. Finally, Fig. A.7 shows that the local oscillator power has a similar effect as the bias voltage. This is because by increasing the LO power, one is effectively increasing the voltage shift. This results in improved non-linear performance as shown before.

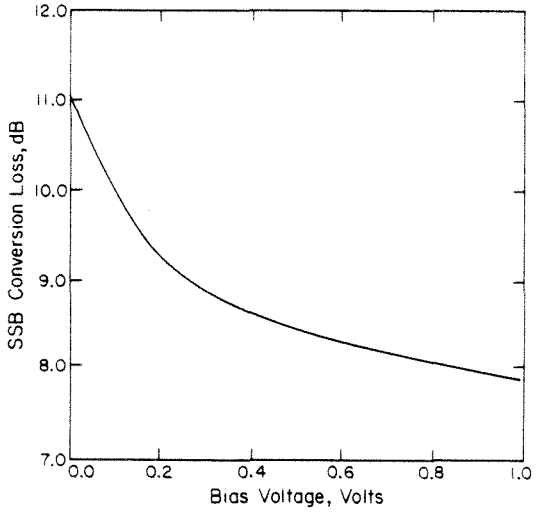

Figure A.6 Conversion loss *vs.* bias voltage for Zah's diode.

Fig. A.8 shows the measured conversion loss and the calculated conversion loss. Zah's diode mixer was simulated by adjusting the device parameters to those measured experimentally, and the circuit parameters to those estimated from the measurement setup. The results show good agreement. The conversion loss in this plot includes the antenna coupling efficiency (about 5dB), and the IF port coupling efficiency.

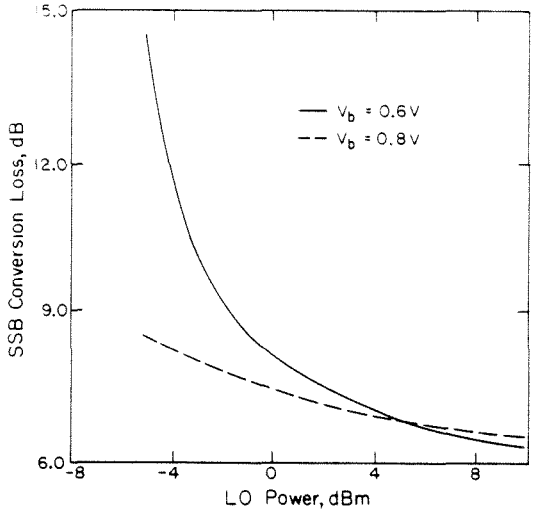

Figure A.7 Conversion loss *vs.* LO power for Zah's diode.

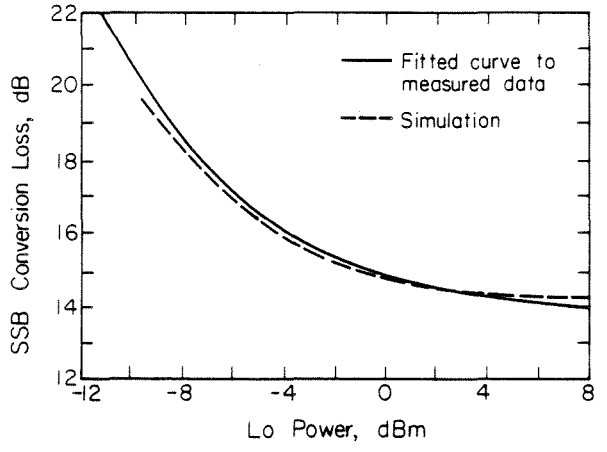

Figure A.8 Measured and calculated conversion loss *vs.* LO power for Zah's diode. The conversion loss includes the antenna coupling loss.

A.3 Conclusion.

The mixer simulation program was shown to be a good analysis tool to study the performance of Schottky diodes mixers. The simulation helps to study the effects of different device and circuit parameters on the mixer performance. Finally, the simulation program was shown to predict experimentally obtainable

results indicating that it is a useful tool for mixer diode design and circuit design.

References.

[1] J. W. Archer, "All Solid-State Low-Noise Receivers for 210-240 GHz," *IEEE Trans. Microwave Theory Tech.*, **MTT-30**, pp. 1247–1252, 1982.

[2] M. A. Frerking *et al.*, "A Broad Band Low-Noise 205 GHz Radiometer for a Satellite Receiver," *Intl. Microwave Symp.*, pp. 110–112, 1983.

[3] N. R. Erickson, "A 200-350 GHz Heterodyne Receiver," *IEEE Trans. Microwave Theory Tech.*, **MTT-29**, pp. 557–561, 1981.

[4] C. E. Zah, "Millimeter-Wave Monolithic Schottky Diode Imaging Arrays," *PhD Thesis Dissertation*, California Institute of Technology, Pasadena, 1985.

[5] D. N. Held, A. R. Kerr, "Conversion Loss and Noise of Microwave and Millimeter-Wave Mixers : Part 1 – Theory," *IEEE Trans. Microwave Theory Tech.*, **MTT-26**, pp. 49–54, 1978.

[6] P. H. Siegel, "Topics in the Optimization of Millimeter-Wave Mixers," *PhD Thesis Dissertation*, Columbia University, New York, 1984.

[7] A. R. Kerr, "A Technique for Determining the Local Oscillator Waveforms in a Microwave Mixer," *IEEE Trans. Microwave Theory Tech.*, **MTT-23**, pp. 828–831, 1975.

[8] A. A. M. Saleh, "Theory of Resistive Mixers," *PhD Thesis Dissertation*, Massachussetts Institute of Technology, Cambridge, 1970.

[9] C. E. Zah, "Millimeter-Wave Monolithic Schottky Diode Imaging Arrays," *Intl. J. Infrared and Millimeter Waves*, **6**, pp. 981–997, 1985.

[10] C. Dragone, "Analysis of Thermal and Shot Noise in Pumped Resistive Diodes," *Bell System Tech. J.*, **47**, pp. 1883–1902, 1968.

[11] A. R. Kerr, "Shot-Noise in Resistive-Diode Mixers and the Attenuator Noise Model," *IEEE Trans. Microwave Theory Tech.*, **MTT-27**, pp. 135-140, 1979.

[12] J. W. Archer, "Millimeter Wavelength Frequency Multipliers," *IEEE Trans. Microwave Theory Tech.*, **MTT-29**, pp. 552–557, 1981.

[13] M. V. Schneider, "Metal-Semiconductor Junction as Frequency Convertors," *Infrared and Millimeter Waves*, **6**, pp. 209–275, K. J. Button ed., Academic Press Inc., New York, 1983.